Broadscale dampening of uncertainty adjustment in the aging brain

Julian Q. Kosciessa[1,2,3]*, Ulrich Mayr[4], Ulman Lindenberger[1,2], & Douglas D. Garrett[1,2]*

[1] Max Planck UCL Centre for Computational Psychiatry and Ageing Research, Berlin and London
[2] Center for Lifespan Psychology, Max Planck Institute for Human Development, Lentzeallee 94, 14195 Berlin, Germany
[3] Radboud University, Donders Institute for Brain, Cognition and Behaviour, Nijmegen, The Netherlands
[4] Department of Psychology, University of Oregon, Eugene, OR 97403, United States

Julian Q. Kosciessa: https://orcid.org/0000-0002-4553-2794
Ulrich Mayr: https://orcid.org/0000-0002-7512-4556
Ulman Lindenberger: https://orcid.org/0000-0001-8428-6453
Douglas D. Garrett: https://orcid.org/0000-0002-0629-7672

0. Abstract

The ability to prioritize task-relevant inputs enables efficient behavior across the human lifespan. However, contexts in which feature relevance is ambiguous require dynamic exploration rather than stable selectivity. Although both cognitive flexibility and stability generally decline with ageing, it is unknown whether the aging brain differentially adjusts to changing uncertainty. Here, we comprehensively assess the dynamic range of uncertainty adjustments across the adult lifespan (N = 100) via behavioral modelling and a theoretically informed set of human neuroimaging signatures (EEG-, fMRI-, and pupil-based). As a group, older adults show a broadscale dampening of neuro-computational uncertainty adjustments. In support of a "maintenance" account of brain aging, older individuals with more young-like neural recruitment were better able to select task-relevant features, also in a Stroop task with low perceptual demands. Our results highlight neural mechanisms whose maintenance plausibly enables flexible task set, perception, and decision computations across the adult lifespan.

1. Introduction

The ability to prioritize goal-related signals in perceptual and decision processes is fundamental for adaptive behaviors. Some contexts facilitate this process by designating features to which we should selectively attend [1]. Many contexts do not convey feature relevance, however. Such elevated uncertainty plausibly shifts demands from an emphasis on focused feature selection to a broad, but less precise sensitivity to diverse candidate features [2,3]. An adaptive system should track the degree of such contextual uncertainty, and leverage it to tune perception, guide decisions, and select actions. Conversely, failure to do so may result in maladaptive cognition and behaviors [4,5]. Here, we examine whether a potential failure to adapt to varying uncertainty is a key characteristic of healthy human aging.

Behavioral observations support aging-related deficits in uncertainty-guided processing. In contexts that cue task-relevant dimensions of compound stimuli, older adults remain sensitive also to irrelevant dimensions [6,7], indicating challenges in stable feature-selection [8-11]. Conversely, older adults show inflexibility when contexts require dynamic feature switches [12-14], and incur substantial "fade-out" costs when transitioning from dynamic to stable single-feature contexts [15]. Such observations suggest that older adults may be stuck in a suboptimal 'middle ground' that neither affords stable task selectivity when uncertainty is low, nor flexible task sensitivity in dynamic or uncertain contexts. Although age-related deficits in using uncertainty variations to guide behavior have been observed to impair computational (learning rate) adjustments [16], it remains unclear whether such underutilization arises from challenges in estimating latent uncertainty, or from leveraging adequate estimates to adjust computations. Crucially, for uncertainty to provide a principled and comprehensive lens on aging-related adaptivity constraints, first evidence is required to establish whether and/or how neural responses to uncertainty differ in the older adult brain.

Although the neural mechanisms of uncertainty resolution remain vague [17], emerging models point to interacting systems that define task sets, alter perception, and guide decision formation [18-20]. Task set management has been commonly tied to fronto-parietal cortex [20,21], although more recent evidence also suggests underappreciated thalamic deep brain contributions especially in uncertain contexts [22,23]. When task sets are limited to specific sensory features, perceptual networks in turn appear to specifically tune to relevant information by combining distractor inhibition [24] with target enhancement [25]. In contrast, high uncertainty may facilitate sensitivity to multiple features via broad excitability increases [26]. Shifts between such regimes may be orchestrated by diffuse neurotransmitter systems that adjust computational precision to changing demands [2]. In young adults, we observed such an integrated response to rising uncertainty [27], encompassing increased fronto-thalamic BOLD activation, increased pupil diameter as an index of neuromodulation [28], and upregulated EEG-based cortical excitability. These results indicate that multiple systems interact to enable a large dynamic response range to contextual uncertainty variations. Whether and how these systems change in their response to uncertainty across the adult lifespan has not been tested, however.

It is plausible that joint declines of these systems are a feature of brain aging, constraining the dynamic range of uncertainty adjustments. Senescence is characterized by various systemic alterations including diminished prefrontal cortex function [29], metabolic decreases in fronto-thalamic control networks [30-32], progressive deterioration of subcortical neurotransmitter systems [33-35], reduced cortical inhibition [36,37], as well as structural declines of coordinating nodes such as the thalamus [38,39]. However, beyond findings that older adults' brain activity changes less alongside varying demands in general [40-42], whether older brains also adjust less to contextual uncertainty is unknown. Beyond the group-level, the "maintenance account of aging" further posits that cognitive deficits with senescence emerge when neural resources become insufficient to meet demands, and that older adults with more "young-like" signatures should be most likely to maintain function. We test this account by examining whether a reduced engagement of neural mechanisms expressed in younger adults constrains the range of uncertainty adaptation in older age.

Here, we use decision modelling and multimodal neuroimaging (EEG, fMRI, pupillometry) in 47 younger and 53 older adults to investigate how contextual uncertainty impacts neural and behavioral computations across the adult lifespan. Participants performed a decision task involving a compound stimulus, for which we overtly manipulated uncertainty regarding the stimulus feature(s) that would be relevant for decisions. By assessing multiple *a priori* signatures that were observed in younger adults' response to contextual uncertainty [27], we observed that older adults exhibited a relatively dampened modulation of decision processes and neural responses to varying contextual uncertainty. Older adults expressing more flexible feature selection were marked by more "young-like" modulation of neural signatures, providing first evidence for a brain maintenance account in the context of uncertainty processing.

2. Results

2.1 Older adults express constrained uncertainty modulation of evidence integration.

During EEG and fMRI acquisition, participants performed a **M**ulti-**A**ttribute **A**ttention **T**ask ("MAAT" [27]; Figure 1a). In the task, participants had to visually sample a moving display of squares that were characterized by four feature dimensions, with two exemplars each: color (red/green), movement direction (left/right), size (large/small), and color saturation (high/low). Stimuli were presented for three seconds, after which participants were probed as to which of the two exemplars of a single feature was most prevalent. Probe uncertainty was parametrically manipulated using valid pre-stimulus cues that indicated the feature set from which a probe would be selected with equal probability. Higher uncertainty necessitated extra-dimensional attention shifts [43,44] between up to four features ("target load") to optimally inform probe-related decisions. Younger and older adults performed the task above chance level for all visual features (Figure S1-1).

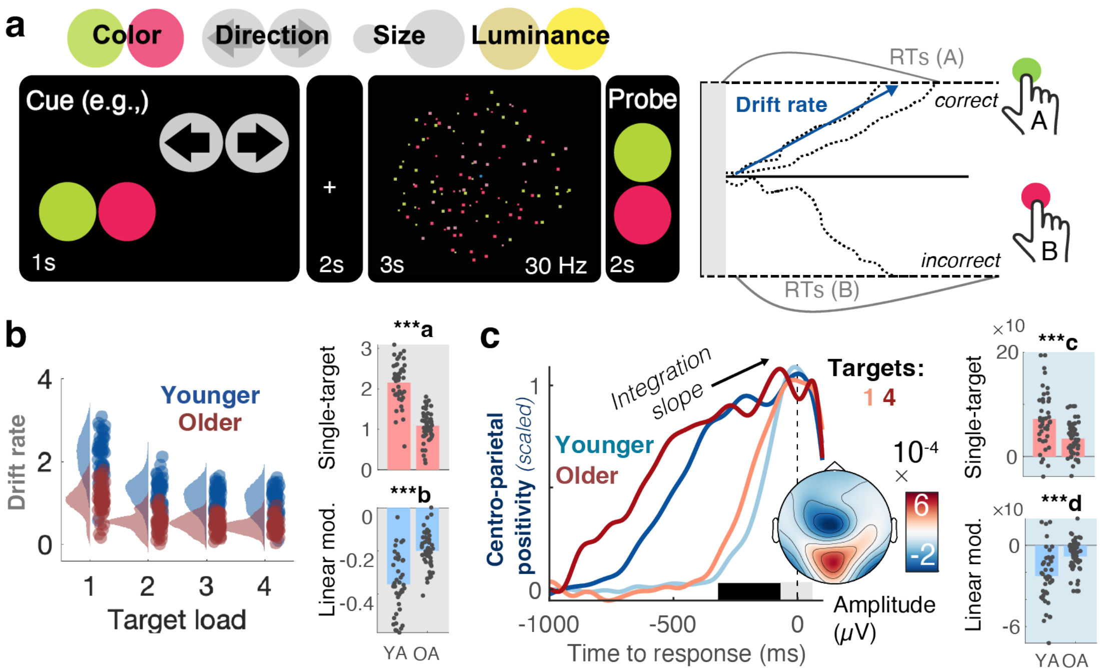

Figure 1. Older adults show constrained decision-related adjustments to rising uncertainty. (a) Participants performed a Multi-Attribute Attention Task ("MAAT") during which they had to sample up to four visual features of a compound stimulus for a subsequent perceptual decision. On each trial, participants were first validly cued to a target probe set (here motion direction and color). The compound stimulus (which always included all four features) was then presented for 3 s and was followed by a probe of one of the cued features (here, whether red or green color was more prevalent in the stimulus). The number of pre-stimulus cues manipulated the level of uncertainty. Behavioral data were modelled with a drift diffusion model, in which evidence is presumed to be successively accumulated with a 'drift rate' towards either of two bounds, here representing the options of a single feature. (b) Drift rate estimates from behavioral modelling. Older adults exhibited reduced accumulation rates for single targes (top) and were marked by more limited drift reductions under elevated uncertainty (bottom). Individual data points represent averages across EEG and fMRI sessions. Table S1 reports within-group statistics. (c) The Centro-parietal positivity (CPP) provides an *a priori* neural signature of evidence accumulation. Older adults exhibited reduced integration slops for single targes (top) and were marked by constrained load-related slope shallowing under elevated uncertainty (bottom). To illustrate age- and condition-differences in integration slope, responses have been rescaled to the [0, 1] range for visualization. Fig. S1-3 shows original traces. *****a** p=0e-10 *****b** p = 5.1e-10 *****c** p = 4.5e-05 *****d** p = 2.8e-05.

To characterize probe-related decision processes, we fitted a hierarchical drift-diffusion model [45] (HDDM) to participants' responses. The model estimates (a) the drift rate at which evidence is integrated towards a decision bound, (b) the distance between (correct and incorrect) decision bounds, and (a) the non-decision time of visual probe processing and response execution. Across sessions and age groups the best fitting models (see Figure S1-2) consistently included uncertainty-based variations in all three parameters. Here, we focused on the drift rate of evidence integration based on its close association to stimulus processing [27]. Text S1-2 reports the remaining parameters. With rising uncertainty, evidence drift rates decreased for both age groups, indicating that uncertainty constrained decision evidence for the probed feature also in older adults. Crucially, relative to younger adults, older participants' drift rates were reduced following single-attribute cues, and decreased less under increasing uncertainty (Figure 1b). These drift rate effects remained present when only features with age-matched single-target accuracies were included in the model (see Text S1-3). However, we also observed that for features matched in single-target accuracy, older adults suffered stronger accuracy decreases under uncertainty than younger adults, in line with a larger behavioral cost of transitioning into more uncertain task contexts (see Text S1-4).

We assessed the convergence of behavioral results with an *a priori* neural proxy signature of evidence integration, the slope of the EEG's centroparietal positive potential (CPP [46]; Figure 1c, see also Figure S1-4) prior to decision responses. Consistent with behavioral modeling, CPP slopes were flatter for older relative to younger participants in single-target contexts, and older adults' uncertainty-related modulation of CPP slopes was minimal (Figure 1c). In line with both indices capturing latent evidence integration, CPP and drift estimates were inter-individually related (Fig. S1-4), both for single targets ($r(93) = 0.51$, 95%CI = [0.34,0.64], $p = 1.4e\text{-}07$; *age-partial:* $r(92) = 0.34$, 95%CI = [0.14,0.5] $p = 9.3e\text{-}04$), and their uncertainty modulation ($r(93) = 0.45$, 95%CI = [0.27,0.59], $p = 6.1e\text{-}06$; *age-partial:* $r(92) = 0.27$, 95%CI = [0.08,0.45], $p = 0.01$; Fig S1-4c). We also probed contralateral beta power as a signature of motor response preparation [47] (Figure S1-5) but did not observe clear relations to drift rate or CPP estimates (Text S1-5), suggesting that it may be a less suitable evidence integration index here. Taken together, older adults' decisions were marked by reduced evidence integration rates for single targets, and more constrained drift rate reductions under uncertainty.

2.2 Decoding indicates uncertainty-induced trade-offs between feature specificity and sensitivity.

Higher single-target drift rates and larger evidence reductions may reflect an adaptive trade-off between reduced single-feature specificity and elevated sensitivity to *multiple* features under higher uncertainty. However, as decisions were tied to the probed feature, they cannot elucidate how unprobed feature dimensions were processed. To clarify this question, we performed fMRI decoding analyses. We created pairwise classifiers that targeted the sensory representation of each feature's prevalent option (e.g., left vs. rightward movement) based on BOLD responses in visual cortex (see *Methods: fMRI decoding of prevalent feature options*). The prevalent option of individual features could be decoded above chance during the approximate time of stimulus presentation (Fig. 2a). Robust decoding was observed for all cued features except for luminance, for which discrimination was also behaviorally most challenging (Fig. S1-1). Above-chance decoding was not observed for uncued feature options, except for motion discrimination (see Fig. 2b), indicating that participants mainly discriminated task-relevant feature options [18].

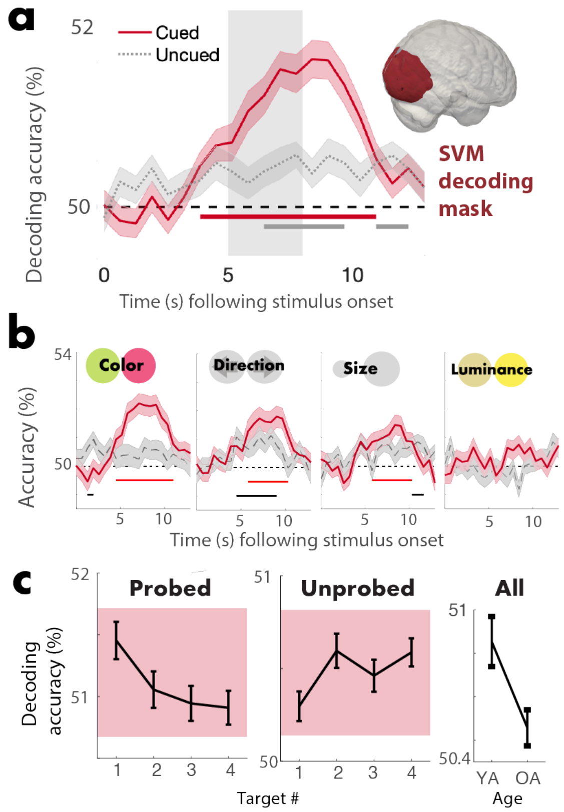

Figure 2. Decoding of prevalent options from visual cortex. (a) Decoding accuracy for cued and uncued features across age groups (means +/- SEM). Grey shading indicates the approximate timing of stimulus presentation considering the temporal lag in the hemodynamic response. Lines indicate periods of statistically significant differences from chance decoding accuracy (50%) as assessed by cluster-based permutation tests. The inset highlights the visual cortex mask from which signals were extracted for decoding. (b) Same as in a, but for each feature probe. (c) Decoding accuracy for probed (left) and unprobed (center) features as a function of the number of cued targets; and decoding accuracy for al features as a function of age (right). Accuracy was averaged across significant decoding timepoints for cued features. Means +- within-subject SEM for (un)probed features, means +- SEM for age analysis.

Next, we assessed uncertainty and age effects on decoding accuracy. First, we applied classifiers to trials in which target features were probed, which mirrors the participant's behavioral task. A linear mixed effects model indicated a significant reduction in decoding accuracy with increasing uncertainty (β = -0.18, SE = 0.05, t = -3.56, p = 0.00037; Figure 2c), as well as reduced decoding accuracy for older adults (β = -0.862, SE = 0.31, t = -2.77, p = 0.007), but no significant interaction (p = 0.76). Crucially, such uncertainty-related precision losses may trade-off against sensitivity to other cued, but ultimately unprobed features. We tested this possibility by considering decoding accuracy across all *unprobed* features in any given trial. This analysis indicated that uncertainty indeed slightly increased decoding accuracy across unprobed features (β = 0.077, SE = 0.026, t = 2.94, p = 0.0033). Decoding accuracy trended to be lower in older compared to younger adults (β = -0.259, SE = 0.134, t = -1.92, p = 0.0574). Again, no significant interaction was observed (p = 0.434). Consistent with opposing uncertainty effects on probed and unprobed features, no significant uncertainty effect was indicated when all trials were considered (β = 0.012, SE = 0.024, t = 0.53, p = 0.5927), but decoding accuracy was overall reduced in older adults (β = -.41, SE = 0.144, t = -2.84, p = 0.0056). Decoding analyses thus suggest that rising uncertainty in both age groups increased sensitivity to more diverse features, albeit at the cost of reduced precision for single features.

2.3 MAAT performance generalizes to feature selection in the context of low perceptual demands.

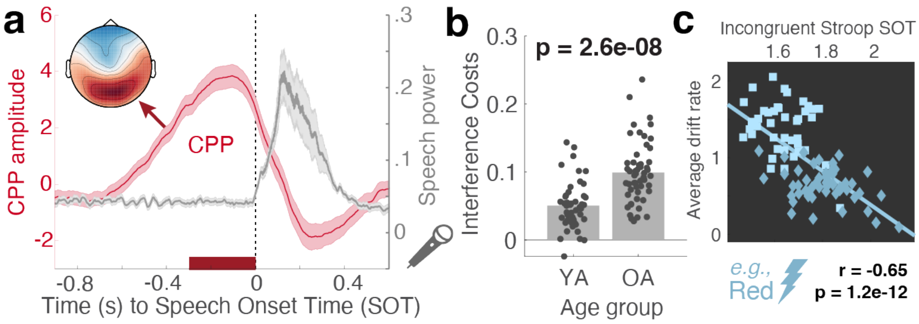

Figure 3. MAAT evidence integration relates to prepotent response inhibition. (a) Centro-Parietal Positivity (CPP) traces and speech signal power suggest high validity for the semi-automatically labeled speech onset times (SOTs). The CPP trace has been averaged across age and congruency conditions and displays means +/- SEM. The inset shows the mean EEG topography during the final 300 ms prior to speech onset. (b) The voiced Stroop task indicated robust interference costs whose magnitude was larger in older adults. Table S1 reports within-group statistics. (c) Participants with larger MAAT drift rates showed faster responses to incongruent trials (e.g., responding blue to the inset stimulus), also after accounting for categorical age (squares: younger; diamonds: older) and covariation with congruent SOTs (see main text).

Relative to younger adults, older adults appear to have encoded less single-target evidence for downstream decisions. However, the multifaceted demands of the MAAT do not resolve whether such differences arise from task idiosyncrasies such as the necessity to resolve high perceptual uncertainty for each feature, or whether they capture differences related to flexible feature selection. To adjudicate between these accounts, participants also performed a Stroop task, which probes the capacity to inhibit prepotent responses to one of two feature dimensions (the color vs. semantics) of a presented word [48]. We recorded voice responses as a more naturalistic modality for older adults [49]. To estimate speech onset times (SOTs ~ reaction times), we labeled the onset of voiced responses in each trial's recording (see methods). Labeled SOTs showed high validity as the neural CPP peaked immediately prior to SOTs (Fig. 3a). In line with the Stroop literature [49], older adults incurred larger behavioral interference costs (Fig. 3b) than younger adults. These behavioral results were mirrored by neural CPP slopes: interference shallowed pre-response CPP slopes in both age groups, but to a larger extent in older adults, and the CPP shallowing tracked behavioral interference costs across subjects (Fig. S3-1). Crucially, participants with higher MAAT drift rates were also faster responders in the incongruent condition (Fig. 3c), pointing to a better capacity to inhibit prepotent responses. Notably, relations between MAAT drift rates and SOTs in the Stroop interference condition (r(93) = -0.65, 95%CI = [-0.75,-0.51], p = 1.2e-12) held after controlling for age and SOTs in the congruent condition (r(91) = -0.29, 95%CI = [-0.46,-0.09], p = 0.01), whereas the opposite was not observed (congruent SOTs-drift: r(93) = -0.4, 95%CI = [-0.56,-0.22], p = 4.7e-05, *age- and incongruent SOT-partial*: r(91) = 0.13, 95%CI = [-0.07,0.33], p = 0.2). As such, selective inhibition of interfering features, as opposed to processing speed, appears to be a key contributor to individual MAAT drift rates. Taken together, these findings suggest that individual and age differences in MAAT drift rates generalize to flexible feature selection also in perceptually unambiguous contexts.

2.4 Theta power and pupil diameter upregulation with elevated uncertainty dampens in older age.

Our results indicate age-related constraints in adjusting perceptual and decision processes to varying uncertainty. To test whether such constraints are rooted in a reduced neural uncertainty response as expected under a maintenance account of cognitive & brain aging, we assessed several *a priori* signatures (see [27]) during MAAT stimulus presentation by means of two-group task partial-least-squares analyses (PLS, see methods). First, we assessed the effect of uncertainty on frontocentral theta power, an index of cognitive control [50] and exploration under uncertainty [51]. Uncertainty increased theta power in both age groups (Figure 4a), but to a lesser extent in older adults (Figure 4a). Next, we assessed phasic changes in pupil diameter, a signature that covaries with neuromodulation and arousal [52,53], has been related to frontal control [2,27,54-56], and is sensitive to rising demands [57] such as dynamically changing and uncertain contexts [58,59]. Once again, we observed that uncertainty increased pupil diameter in both age groups, with more constrained upregulation in older adults (Fig. 4b). The extent of pupil modulation was related to individual theta power increases ($r(98) = .28$, 95%CI = [0.09, 0.46], $p = 0.005$; *age-partial*: $r(97) = .19$, 95%CI = [0, 0.38], $p = 0.05$), indicating a joint uncertainty modulation. These results indicate that both age groups were sensitive to rising uncertainty, albeit older adults to a dampened extent.

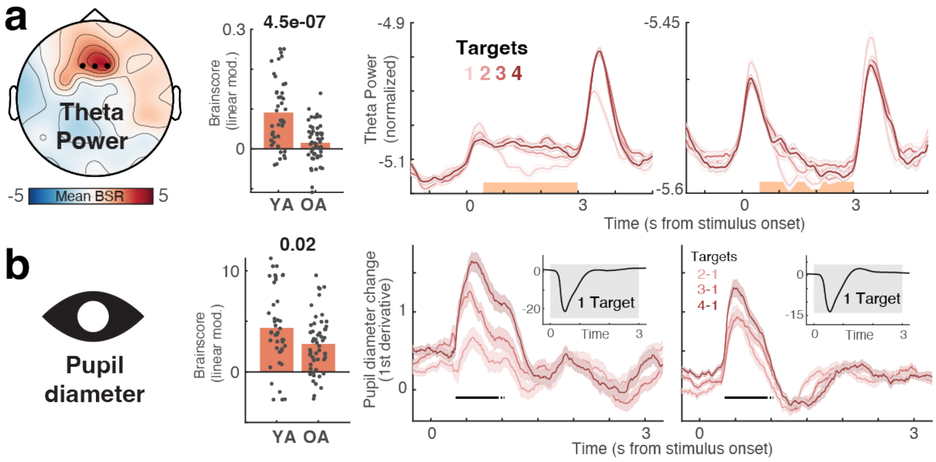

Figure 4. Uncertainty increases theta power (a) and pupil diameter (b) across the adult lifespan. (Center) Age comparison of linear uncertainty effects (~age x target load interaction). Red bars indicate significant within-group differences from zero, as assessed via one-sample t-tests (see Table S1). Both signatures exhibited significant uncertainty modulation in younger, as well as older adults, with constrained modulation in older adults. For condition-wise plots, see Fig. S4-1. Statistics refer to unpaired t-tests. (Right) Time series data are presented as means +- within-subject S.E.Ms. Orange shading in a indicates the timepoints across which data have been averaged for the task PLS. Black lines in b indicate time points exceeding a BSR of 3 (~99% threshold). The uncertainty modulation of pupil diameter occurred on top of a general pupil constriction due to stimulus-evoked changes in luminance upon task onset (see inset), that by stimulus design did not systematically differ across load levels. YA = Younger adults. OA = Older adults.

2.5 Only younger adults adjust posterior cortical excitability to varying uncertainty.

Elevated contextual uncertainty may impact perception by altering sensory excitability. To test this, we focused on three indices related to cortical excitability: alpha power, sample entropy, and aperiodic 1/f slopes [27,60]. We constrained analyses to posterior sensors as we targeted perceptual changes in visual-parietal cortices. *Text S5-3* reports whole-

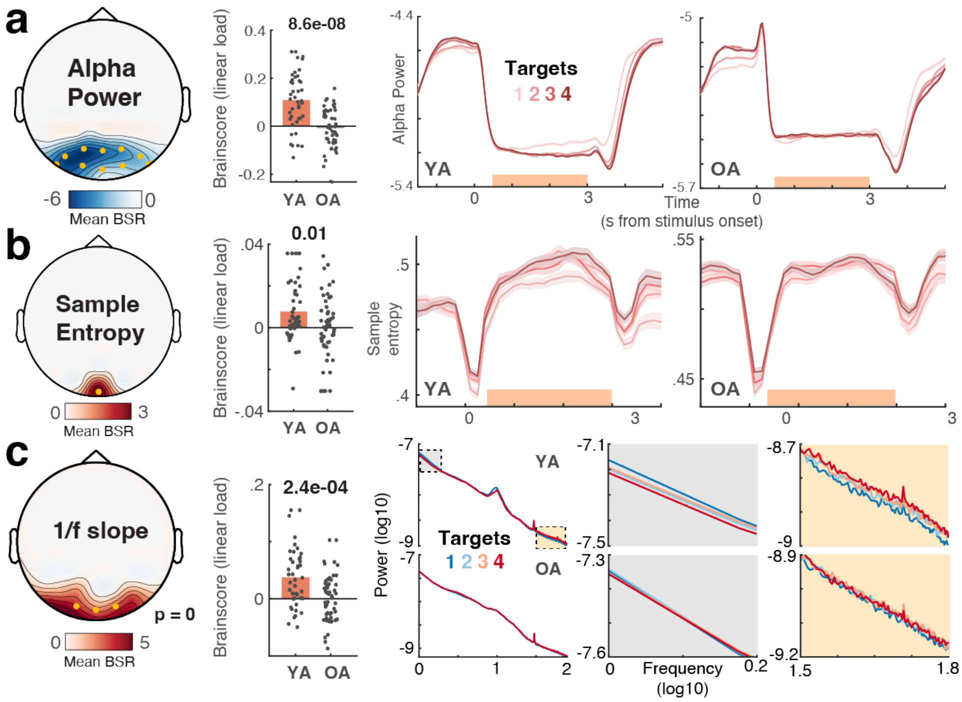

Figure 5. Only younger adults upregulate cortical excitability under increased uncertainty. (a-c) Results of task partial least squares (PLS) models, assessing relations of alpha power (a), sample entropy (b) and aperiodic 1/f slope (c) to uncertainty. (Left) Topographies indicate mean bootstrap ratios (BSR). Orange dots indicate the sensors across which data were averaged for data visualization. (Center) Age comparison of linear uncertainty effects (~age x uncertainty interaction). All three signatures exhibited a significant uncertainty modulation in younger, but not in older adults. For condition-wise plots, see Fig. S4-1. Statistics refer to unpaired t-tests. Table S1 reports within-group statistics. (Right) Time series data are presented as means +- within-subject S.E.Ms. Orange shading in a indicates the timepoints across which data have been averaged for the respective task-PLS. Black lines in b indicate time points exceeding a BSR of 3 (~99% threshold). YA = Younger adults. OA = Older adults.

channel analyses. In younger adults, we observed uncertainty effects on all three signatures (Fig. 5 a-c), akin to those we previously reported [27]. In line with putative excitability increases, posterior alpha power decreased alongside uncertainty, while sample entropy increased and the aperiodic spectral slope shallowed. However, we found no evidence of a similar modulation in older adults for any of the probed signatures (Fig. 5, see also Fig. S4-1), indicating a failure of the aged system to adjust to changing uncertainty demands. Such failure may be rooted in a less precise estimation of environmental uncertainty in the aged neural system [16]. However, we reduced inference demands in our design by providing overt cues on each trial, and keeping the cue set identical for eight consecutive trials. In line with age-invariant sensitivity to uncertainty cues, we observed comparable increases in pre-stimulus alpha power alongside uncertainty in both age groups (Fig. S5-1, see also Text S5-1). However, these increases were not associated with subsequent behavioral drift rate adjustments (Fig. S5-1 and Text S5-1), arguing against a direct role of pre-stimulus alpha power in adjudicating uncertainty. We additionally considered the steady-state visual evoked potential (SSVEP) as a proxy of bottom-up processing. Despite robust and comparable SSVEPs in both age groups, we found no evidence of uncertainty modulation in either group (Fig. S5-2, see also Text S5-2). Given that the 30 Hz flicker frequency was shared between all stimulus features, this suggests that sensory processing of the compound stimulus was similar between uncertainty conditions and age groups. Taken together, our results suggest that older adults may have suffered from a relative failure to adjust perceptual excitability to changing feature relevance, rather than insensitivity to the level of contextual uncertainty or an inability to encode the undifferentiated stimulus.

2.6 BOLD modulation links neuro-behavioral responses to uncertainty across the adult lifespan.

Finally, we investigated uncertainty-related changes in whole-brain fMRI BOLD activation during stimulus presentation, extending sensitivity also to subcortical areas like the thalamus that are considered critical for managing contextual uncertainty [27,61,62]. We targeted associations between uncertainty-related BOLD modulation and the *a priori* neurobehavioral signatures (i.e., uncertainty-induced changes in drift rate, theta power, pupil diameter, alpha power,

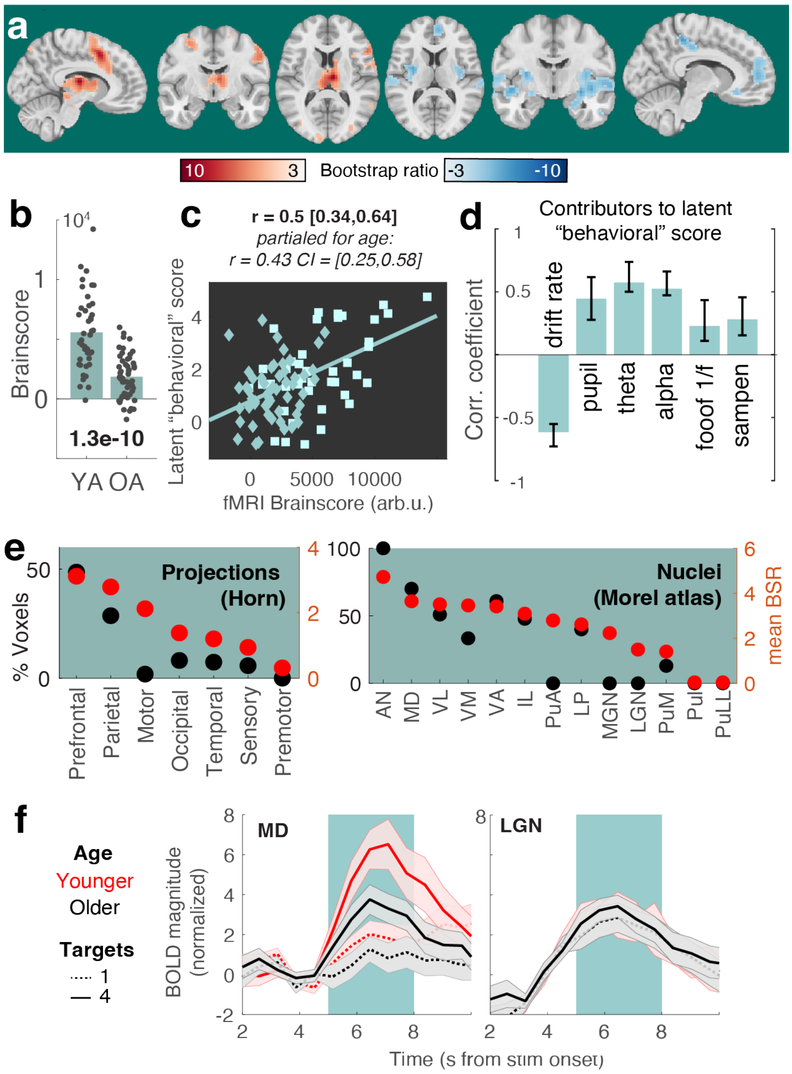

Figure 6: Multivariate relation of EEG/pupil/behavioral signatures to fMRI BOLD uncertainty modulation. (a) Results of a behavioral partial least squares (PLS) analysis linking linear changes in BOLD activation to interindividual EEG, pupil, and behavioral differences. Table S4 lists peak coordinates. (b) The multivariate expression of BOLD changes alongside rising uncertainty was reduced in older compared with younger adults. Table S1 reports within-group statistics. (c) Individual Brainscore differences were related to a behavioral composite score, also after accounting for age covariation. Squares = younger individuals; diamonds = older individuals. (d) Signature-specific Brainscore relations. All signature estimates refer to linear changes as a function of uncertainty. Error bars represent bootstrapped 95% confidence values. (e) Major nuclei and projection zones in which behavioral relations are maximally reliable according to average Bootstrap ratios (red) and the percentage of voxels in each subregion exceeding a BSR of 3. See Methods for abbreviations. Strongest expression is observed in nuclei that project to fronto-parietal cortical targets. (f) Visualization of uncertainty modulation for the mediodorsal nucleus, a "higher order" nucleus, and the LGN, a visual relay nucleus. Traces display mean +/- SEM. The green shading indicates the approximate stimulus presentation period after accounting for the delay in the hemodynamic response function.

1/f slopes, and sample entropy) using a multivariate behavioral PLS analysis (see *Methods*; Text S4-1 reports a task PLS targeting the main effect of uncertainty). We identified a single latent variable (LV; *permuted* $p < 1e-3$) with positive frontoparietal and thalamic loadings, and most pronounced negative loadings in medial PFC and hippocampus (Fig. 6a, Table S5). Older adults expressed this LV to a lesser extent than younger adults as indicated by lower "Brainscores" (Fig. 6b), indicating dampened BOLD modulation in the face of changing uncertainty. Brainscores were associated with the latent score of neurobehavioral input signatures (Fig. 6c), such that less dampened, more "young-like" BOLD modulation tracked a larger modulation of decision, EEG, and pupil signatures. Fig. 6d depicts relations to the individual signatures of the model: across age groups, greater BOLD modulation corresponded to larger drift rate reductions, more pronounced theta power and pupil diameter increases, and larger excitability modulation (see Fig. S6-2 for more signatures). As the PLS model leveraged variance both from within and across age groups, we used linear-mixed-effects models to assess the age-dependency of these relations. These models indicated that all *a priori* signatures, except sample entropy and 1/f modulation, predicted Brainscores also after accounting for the shared main effects of age (Table 1). This indicates a robust coupling of uncertainty effects between most signatures, while aligning with unobserved posterior excitability modulation in older adults. Control analyses indicate that within- and between-group differences in BOLD uncertainty sensitivity are robust to matched feature accuracy (see Fig S6-3).

Predictor	**t-value**	**p-value**	**partial η^2**
Behavioral score	4.6043	**1.3237e-05**	0.1962
age	-6.3809	**7.0027e-09**	0.3192
Drift mod.	-4.3334	**3.7435e-05**	0.2308
age	-3.9624	**0.00014637**	0.2006
Pupil mod.	4.171	**6.86e-05**	0.1622
age	-6.7664	**1.2032e-09**	0.3375
Theta mod.	4.2533	**5.0549e-05**	0.2005
age	-4.8662	**4.6912e-06**	0.2471
Alpha mod.	3.2185	**0.0017805**	0.1294
age	-4.934	**3.569e-06**	0.2589
1/f mod.	0.10914	0.91333	1.4502e-04
age	-6.7591	**1.2445e-09**	0.3574
SampEn mod.	1.5944	0.11429	0.0279
age	-6.7385	**1.368e-09**	0.3390

Table 1: Summary of Brainscore predictors, while controlling for categorical age. Separate linear-mixed-effects models assessed effects of target signature, categorical age, and age x signature interactions on Brainscores. We observed no significant interaction in any of the models (all $p > 0.05$), pointing to consistent relations across age groups; therefore, all reported models only include main effects of signature and age. Fig. S6-2 reports similar results using partial regressions. Degrees of freedom: 92 in all models.

Behavioral relations were closely tracked by BOLD activation in the thalamus. To obtain insights within this differentiated structure, we assessed regional loadings based on projection zones and nucleus segmentations (Fig, 6e). Loadings were highest in subregions with frontoparietal projections, including the mediodorsal nucleus (Fig. 6f). In contrast, a traditional visual "relay" nucleus of the thalamus, the lateral geniculate nucleus, did not show sensitivity to our uncertainty manipulation (Fig. 6f). This indicates a specificity of thalamic effects that coheres with functional subdivisions and alludes to uncertainty-invariant sensory processing of the compound stimulus. These results indicate that the mediodorsal thalamus contributes to maintained uncertainty adjustments across the adult lifespan.

3. Discussion

Managing uncertainty is vital for navigating the flux of life. While some environments prioritize specific inputs over others, many contexts provide few, contrasting, or ambiguous cues. Here, we show that healthy older adults exhibit markedly dampened adaptations to such varying uncertainty across coupled EEG/fMRI/pupil signatures. Our results extend observations that older adults rely less on uncertainty representations to guide internal computations [16] by characterizing several plausible neural mechanisms for this shortfall. Our results suggest that such computational constraints do not exclusively stem from an inadequate sensitivity to latent uncertainty, as the current task provides overt uncertainty cues that are similarly processed by both age groups. Rather, our findings support the "maintenance" account of cognitive/brain aging [63] in the context of uncertainty processing, wherein individuals with a more "young-like" neural recruitment are better able to leverage comparable uncertainty estimates to adjust ongoing computations.

3.1 Fronto-thalamic circuits may enable stable and flexible feature selection across the adult lifespan.

As part of the neural uncertainty response, we observed a behaviorally relevant upregulation of anterior cingulate cortex (ACC) BOLD activation and (presumably ACC-based [50,64]) mediofrontal theta power. By charting the progression through multiple task contexts [65-67], the ACC can estimate contextual volatility [68] and uncertainty [16,69] to guide exploration of alternative goals, strategies, and attentional targets [51,70-72]. Non-human animal studies suggest that high contextual uncertainty switches ACC dynamics to a state of increased excitability [60,73] and stochastic activity [74], which benefits concurrent sensitivity to alternate task rules [75]. Also in humans, the ACC is sensitive to stimulus features before they behaviorally guide task strategies [74,76], suggesting that the ACC contributes to the exploration of alternate features whose significance remains contextually unclear [77,78]. While our results align with such contribution, we also localize high uncertainty sensitivity in the mediodorsal (MD) thalamus, which aligns with the MD being a key partner for selecting, switching, and maintaining cortical task representations [23,79,80] especially in uncertain contexts [27,61,62]. Extrapolating from this emerging perspective, the MD-ACC circuit may regulate task set stability vs. flexibility [81-83] according to contextual demands (Fig. 7a). Partial evidence for such a notion is provided by models that link task stability in low-uncertainty contexts to thalamic engagement [84]. The current observations suggest a complementary thalamic role in task flexibility. While maintained across the adult lifespan, BOLD and theta power signals indicated that such MD-ACC upregulation was dampened in older adults [85,86]. Indeed, the ACC network is particularly susceptible to age-related metabolic declines [30-32] as well as structural atrophy [38]. Retained ACC function on the other hand is a hallmark of cognitive reserve [87], relates to maintained executive function [32], and is a fruitful target of cognitive interventions in older adults [86]. Given evidence of a key role of the MD thalamus in the coordination of ACC engagement and our observations of reduced MD-ACC sensitivity to uncertainty in older age, the thalamus may be an underappreciated site for cascading age-related dysfunctions in cognitive stability and flexibility.

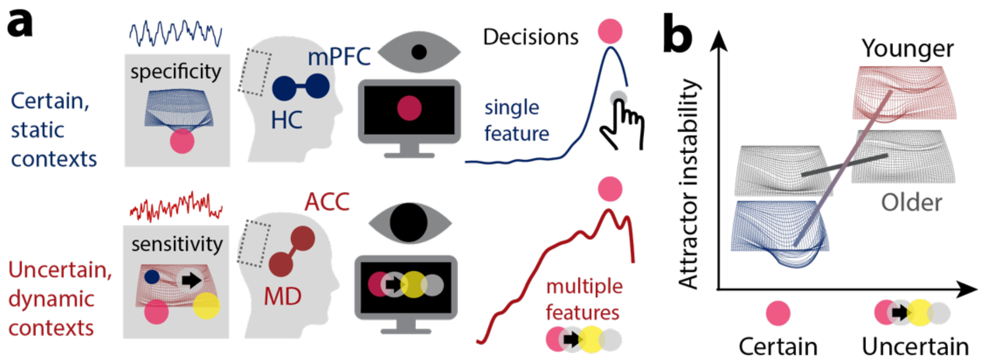

Figure 7. Schematic model summary. (a) In static contexts, prefrontal-hippocampal networks may signal high confidence in the current task state, which enables stable task sets, and a targeted processing of specific sensory representations with high acuity. Such selective processing of specific task-relevant features benefits their efficient evidence integration. Such selectivity would be suboptimal in contexts with uncertain or changing task sets, however. An MD-ACC circuit may track such uncertainty and enhance stochastic task set flexibility in changing or ambiguous contexts. In coordination with posterior-parietal cortex, this feasibly enables more diverse albeit less precise perceptual representations. (b) The neural system of younger adults adjusts system dynamics to the degree of environmental uncertainty. Observed effects align with a switch between a specific processing of individual features with high acuity, as exemplified by a single, deep attractor (blue), and a more diverse, if less precise processing of multiple features, as indicated by a more unstable attractor landscape (red; see also Thiele & Bellgrove, 2018). In contrast, the aged neural system may be stuck in a suboptimal middle ground that affords neither stable precision, nor flexible imprecision. mPFC = medial prefrontal cortex; HC = hippocampus; ACC = anterior cingulate cortex; MD = mediodorsal thalamus.

3.2 Neuromodulation may sculpt the dynamic range of uncertainty adjustments.

Neurotransmitter systems provide a candidate substrate for computational adjustments under uncertainty. In response to rising uncertainty, phasic norepinephrine release can sensitize the system to incoming signals [88,89] by increasing neuro-behavioral activation [52,90]. Pupil diameter, an index that is partially sensitive to noradrenergic drive [57], robustly increases alongside uncertainty during learning [58] and attention [91], environmental exploration [92], and change points in dynamic environments [58,59,93]. Here, we show that such pupil sensitivity to rising uncertainty is retained across the adult lifespan, but dampens in older age. Such dampening hints at declining noradrenergic responsiveness in older age [94,95], arising from reduced LC integrity [96], and/or decreased LC recruitment. Notably, pupil sensitivity to volatility has been related to the ACC as a primary source of cortical LC input [28,97], and joint modulation of ACC and pupil diameter in uncertain, or dynamic contexts has consistently been observed in studies that record both signals [2,27,54-56]. While future studies need to clarify the origin of constrained pupil adjustments in older age, our results affirm the relevance of the extended LC system for attentional function across the lifespan [95]. In contrast to noradrenaline's potential role in sensitizing, cholinergic innervation from the basal forebrain may foster selectivity via cortical gain increases [98,99]. Notably, basal forebrain BOLD activation decreased under uncertainty alongside regions such as the medial prefrontal cortex and hippocampus, that are sensitive to subjective confidence [100], suggesting that it may support stable task beliefs when contextual uncertainty is low [101] (Fig. 7a). The constrained BOLD modulation observed in older adults may thus point to reduced task set stability in low-uncertainty contexts (Fig. 7b) [11], plausibly as a consequence of limited cholinergic gain control. Similar ideas have been captured in the cortical gain theory of aging [102], but in the context of the dopamine system [34,103]. Computational models and pharmacological studies indeed support a role of dopamine availability in task set stability and flexibility [104,105]. For instance, amphetamines (operating via the DA system) can in- and decrease task set stability in ACC [106,107] depending on baseline dopamine levels in frontoparietal cortex and thalamus [108]. Given that our results align with the fronto-thalamic system being a primary neural substrate of cognitive aging [34,39,109], the potential contribution of age-related dopamine depletion to constrained uncertainty adjustments deserves future clarification.

3.3 Excitability modulation as a mechanism for acuity/sensitivity trade-offs.

Uncertain contexts motivate perceptual exploration over a selective encoding of individual features. Our decoding results indeed indicate that higher uncertainty benefitted sensitivity to multiple features at the cost of feature-specific precision (or "acuity") [3]. Perceptual representations thus depend on whether a feature is included in the active task set [18], but also on the degree of competition with other task set elements for neuro-computational resources [110]. Excitability changes in parietal/sensory cortices provide a candidate mechanism that may implement such trade-off. One index of (decreased) cortical excitability is alpha power. Models suggest that broad alpha power increases reflect active inhibition of irrelevant information [111-115], while alpha desynchronization in target regions can selectively disinhibit relevant information [38]. With advancing adult age, alpha power decreases, which has been linked to inhibitory deficits in older age [95,116-119] . Such filtering deficits manifest in maladaptive sensitivity also to irrelevant [7] and non-salient features [120] of compound stimuli [6] that impairs selective feature discrimination as required in the MAAT. Decoding and decision analyses indeed indicate that older adults' task performance suffered from reduced single-feature information, in line with filtering deficits [121,122]. Alpha desynchronization, in turn, is thought to reflect increased sensitivity to multiple input features [26]. In line with such a notion, stronger alpha suppression is observed when multiple features must be jointly tracked [123,124] and retained in working memory [125-128]. In addition to alpha power, aperiodic dynamics such as the spectral slope of the EEG potential [129] and signal entropy [130] may also index levels of neural excitability [60,129]. Here, we reproduce the observation that uncertainty increases excitability as assessed by all three signatures in younger adults [27], but find no evidence for a comparable modulation in older adults. Such deficits in excitability modulation may be rooted in age-related declines of GABAergic inhibition [36,37]. Aperiodic dynamics at rest suggest increased excitatory tone with increased adult age [131-133], including in the current sample [130]. Our results suggest that such imbalances [134] may constrain the dynamic range of excitability modulation in older age, both on- and off-task [42,135]. Ultimately, this may point to dual challenges in implementing selective attention, as well as diverse feature coding under uncertainty (Fig. 7b). It is also possible that the consistently high level of perceptual uncertainty, i.e., the difficulty of arbitrating between the two options of each feature, was overly taxing especially for older participants. Based on behavioral and decoding results, younger adults were indeed better able to arbitrate feature-specific options at all levels of contextual uncertainty, relative to older adults. In this scenario, preserved excitability modulation may be observed if individual features were perceptually less uncertain. However, performance on the Stroop task suggests that age-related deficits (and individual differences) in feature selection generalize to contexts of low perceptual uncertainty. As perceptual uncertainty resolution relies on partially dissociable circuits from those implicated in feature selection [136-138], future work needs to chart the ability to resolve either type across the lifespan.

3.4 Conclusion

Changes in uncertainty provide an important signal that adaptive systems can use to adjust their internal computations. We highlight that such uncertainty-related adjustments present a principled challenge for the aged brain. Our results thus argue that uncertainty provides a useful lens on healthy cognitive aging and underline the need to better understand the integrated neural basis of estimating and computationally leveraging uncertainty signals across the lifespan.

Online Methods

Sample. 47 healthy young adults (mean age = 25.8 years, SD = 4.6, range 18 to 35 years; 25 women) and 53 healthy older adults (mean age = 68.7 years, SD = 4.2, range 59 to 78 years; 28 women) performed a perceptual decision task during 64-channel active scalp EEG acquisition. 42 younger adults and all older adults returned for a subsequent 3T fMRI session. Participants were recruited from the participant database of the Max Planck Institute for Human Development, Berlin, Germany (MPIB). Participants were right-handed, as assessed with a modified version of the Edinburgh Handedness Inventory [139], and had normal or corrected-to-normal vision. Participants reported to be in good health with no known history of neurological or psychiatric incidences, and were paid for their participation (10 € per hour). All older adults had Mini Mental State Examination (MMSE) [140,141] scores above 25. All participants gave written informed consent according to the institutional guidelines of the Deutsche Gesellschaft für Psychologie (DGPS) ethics board, which approved the study.

Procedure: EEG Session. Participants were seated 60 cm in front of a monitor in an acoustically and electrically shielded chamber with their heads placed on a chin rest. Following electrode placement, participants were instructed to rest with their eyes open and closed, each for 3 minutes. Afterwards, participants performed a Stroop task (see below), followed by the visual attention task instruction & practice (see below), the performance of the task and a second Stroop assessment. Stimuli were presented on a 60 Hz 1920x1080p LCD screen (AG Neovo X24) using PsychToolbox 3.0.11 [142-144]. The session lasted ~3 hours. EEG was continuously recorded from 60 active (Ag/AgCl) electrodes using BrainAmp amplifiers (Brain Products GmbH, Gilching, Germany). Scalp electrodes were arranged within an elastic cap (EASYCAP GmbH, Herrsching, Germany) according to the 10% system [145], with the ground placed at AFz. To monitor eye movements, two additional electrodes were placed on the outer canthi (horizontal EOG) and one electrode below the left eye (vertical EOG). During recording, all electrodes were referenced to the right mastoid electrode, while the left mastoid electrode was recorded as an additional channel. Online, signals were digitized at a sampling rate of 1 kHz. In addition to EEG, we simultaneously tracked eye movements and assessed pupil diameter using EyeLink 1000+ hardware (SR Research, v.4.594) with a sampling rate of 1kHz.

Procedure: MRI session. A second testing session included structural and functional MRI assessments. First, participants took part in a short refresh of the visual attention task ("MAAT", see below) instructions and practiced the task outside the scanner. Then, participants were placed in the TimTrio 3T scanner and were instructed in the button mapping. We collected the following sequences: T1w, task (4 runs), T2w, resting state, DTI, with a 15 min out-of-scanner break following the task acquisition. The session lasted ~3 hours. Whole-brain task fMRI data (4 runs á ~11,5 mins, 1066 volumes per run) were collected via a 3T Siemens TrioTim MRI system (Erlangen, Germany) using a multi-band EPI sequence (factor 4; TR = 645 ms; TE = 30 ms; flip angle 60°; FoV = 222 mm; voxel size 3x3x3 mm; 40 transverse slices. The first 12 volumes (12 × 645 ms = 7.7 sec) were removed to ensure a steady state of tissue magnetization (total remaining volumes = 1054 per run). A T1-weighted structural scan (MPRAGE: TR = 2500 ms; TE = 4.77 ms; flip angle 7°; FoV = 256 mm; voxel size 1x1x1 mm; 192 sagittal slices) and a T2-weighted structural scan were also acquired (GRAPPA: TR = 3200 ms; TE = 347 ms; FoV = 256 mm; voxel size 1x1x1 mm; 176 sagittal slices).

The multi-attribute attention task ("MAAT"). The MAAT requires participants to sample up to four visual features in a compound stimulus, in the absence of systematic variation in bottom-up visual stimulation (see Figure 1). Participants were shown a dynamic square display that jointly consisted of four attributes: color (red/green), movement direction (left, right), size (small, large) and saturation (low, high). The task incorporates features from random dot motion tasks which have been extensively studied in both animal models [146-148] and humans [46,149]. Following the presentation of these displays, a probe queried the prevalence of one of the four attributes in the display (e.g., whether the display comprised a greater proportion of either smaller or larger squares) via 2-AFC (alternative forced choices). Prior to stimulus onset, a varying number of valid cues informed participants about the active feature set, out of which one feature would be chosen as the probe. We parametrically manipulated uncertainty regarding the upcoming probe by systematically varying the number of cues between one and four.

The perceptual difficulty of each feature was determined by (a) the fundamental feature difference between the two alternatives and (b) the sensory evidence for each alternative in the display. For (a) the following values were used: high (RGB: 128, 255, 0) and low saturation green (RGB: 192, 255, 128) and high (RGB: 255, 0, 43) and low saturated red (RGB: 255, 128, 149) for color and saturation, 5 and 8 pixels for size differences and a coherence of .2

for directions. For (b) the proportion of winning to losing option (i.e., sensory evidence) was chosen as follows: color: 60/40; direction: 80/20; size: 65/35; luminance: 60/40. Parameter difficulty was established in a pilot population, with the aim to produce above-chance accuracy for individual features. Parameters were held constant across age groups to retain identical bottom-up inputs.

The experiment consisted of four runs of ~10 min, each including eight blocks of eight trials (i.e., a total of 32 trial blocks; 256 trials). The size and constellation of the cue set was held constant within eight-trial blocks to reduce set switching and working memory demands. At the onset of each block, the valid cue set, composed of one to four target features, was presented for 5 s. Each trial was structured as follows: recuing phase (1 s), fixation phase (2 s), dynamic stimulus phase (3 s), probe phase (incl. response; 2 s); ITI (un-jittered; 1.5 s). At the offset of each block, participants received performance feedback for 3 s. The four attributes spanned a constellation of 16 feature combinations (4x4), of which presentation frequency was matched within participants. The size and type of the cue set was pseudo-randomized: Within each run, every set size was presented once, but never directly following a block of the same set size. In every block, each feature in the active set acted as a probe in at least one trial. Moreover, any attribute served as a probe equally often across blocks. The dominant options for each feature were counterbalanced across all trials of the experiment. To retain high motivation during the task and encourage fast and accurate responses, we instructed participants that one response would randomly be drawn at the end of each block; if this response was correct and faster than the mean RT during the preceding block, they would earn a reward of 20 cents. However, we pseudo-randomized feedback such that all participants received an additional fixed payout of 10 € per session. This bonus was paid at the end of the second session, at which point participants were debriefed.

Stroop performance. Participants performed a voiced Stroop task before and after the main MAAT task in the EEG session. EEG signals were acquired during task performance. One subject did not complete the second Stroop acquisition. In the Stroop task, we presented three words (RED, GREEN, BLUE) either in the congruent or incongruent display color. Each of the two runs consisted of 81 trials, with fully matched combinations, i.e., 1/3rd congruent trials. Stimuli were presented for two seconds, followed by a one-second ITI with a centrally presented fixation cross. Participants were instructed to indicate the displayed color as fast and accurately as possible following stimulus onset by speaking into a microphone. During analysis, speech on- and offsets were pre-labeled automatically using a custom tool (**C**omputer-**A**ssisted **R**esponse **L**abeler (CARL); doi: 10.5281/zenodo.7505622), and manually inspected and refined by one of two trained labelers. Voiced responses were manually labeled using the CARL GUI. Speech onset times (SOTs) were highly reliable across two Stroop sessions preceding and following the MAAT (r = .83, p =5e-26), as were individual interference costs (r = .64, p =5e-13). We therefore averaged SOTs estimates across both runs, where available. For EEG analyses, single-trial time series were aligned to SOTs, and averaged according to coherence conditions. The centroparietal positive potential was extracted from channel POz, at which we observed a maximum potential during the average 300 ms prior to SOT (see inset in Fig. 3a).

Behavioral estimates of probe-related decision processes. Sequential sampling models, such as the drift-diffusion model, have been used to characterize evolving perceptual decisions in 2-alternative forced choice (2AFC) random dot motion tasks [46], memory retrieval [150], and probabilistic decision making [151]. We estimated individual evidence integration parameters within the HDDM 0.6.0 toolbox [45] to regularize relatively sparse within-subject data with group priors based on a large number of participants. Premature responses faster than 250 ms were excluded prior to modeling, and the probability of outliers was set to 5%. 7000 Markov-Chain Monte Carlo samples were sampled to estimate parameters, with the first 5000 samples being discarded as burn-in to achieve convergence. We judged convergence for each model by visually assessing both Markov chain convergence and posterior predictive fits. Individual estimates were averaged across the remaining 2000 samples for follow-up analyses. We fitted data to correct and incorrect RTs (termed 'accuracy coding' in Wiecki, et al. [45]). To explain differences in decision components, we compared four separate models. In the 'full model', we allowed the following parameters to vary between conditions: (i) the mean drift rate across trials, (ii) the threshold separation between the two decision bounds, (iii) the non-decision time, which represents the summed duration of sensory encoding and response execution. In the remaining models, we reduced model complexity, by only varying (a) drift, (b) drift + threshold, or (c) drift + NDT, with a null model fixing all three parameters. For model comparison, we first used the Deviance Information Criterion (DIC) to select the model which provided the best fit to our data. The DIC compares models based on the maximal log-likelihood value, while penalizing model complexity. The full model provided the best fit to the empirical data based on the DIC index (Figure S1c) in both the EEG and the fMRI session, and in either age group. Posterior predictive checks indicated a suitable recovery of behavioral effects using this full solution. Given the observation of high reliability between sessions [27] (see also Figure S1-2), we averaged parameter estimates across the EEG and fMRI sessions for the main analysis. In contrast with previous work [27], we did not constrain boundary separation estimates [152] here given our observation of CPP threshold differences in older adults (see Figure S1-3a). See also Text 1-2 for a brief discussion of NDT and boundary separation.

EEG preprocessing. Preprocessing and analysis of EEG data were conducted with the FieldTrip toolbox (v.20170904) [153] and using custom-written MATLAB (The MathWorks Inc., Natick, MA, USA) code. Offline, EEG data were filtered using a 4th order Butterworth filter with a passband of 0.5 to 100 Hz. Subsequently, data were downsampled to 500 Hz and all channels were re-referenced to mathematically averaged mastoids. Blink, movement and heart-beat artifacts were identified using Independent Component Analysis (ICA; [154]) and removed from the signal. Artifact-contaminated channels (determined across epochs) were automatically detected using (a) the FASTER algorithm [155], and by (b) detecting outliers exceeding three standard deviations of the kurtosis of the distribution of power values in each epoch within low (0.2-2 Hz) or high (30-100 Hz) frequency bands, respectively. Rejected channels were interpolated using spherical splines [156]. Subsequently, noisy epochs were likewise excluded based on a custom implementation of FASTER and on recursive outlier detection. Finally, recordings were segmented to stimulus onsets and were epoched into separate trials. To enhance spatial specificity, scalp current density estimates were derived via 4th order spherical splines [156] using a standard 1005 channel layout (conductivity: 0.33 S/m; regularization: 1^-05; 14th degree polynomials).

Electrophysiological estimates of probe-related decision processes.

Centro-Parietal Positivity (CPP). The Centro-Parietal Positivity (CPP) is an electrophysiological signature of internal evidence-to-bound accumulation [46,152,157]. We probed the task modulation of this established signature and assessed its convergence with behavioral parameter estimates. To derive the CPP, preprocessed EEG data were low-pass filtered at 8 Hz with a 6th order Butterworth filter to exclude low-frequency oscillations, epoched relative to response and averaged across trials within each condition. In accordance with the literature, this revealed a dipolar scalp potential that exhibited a positive peak over parietal channel POz (Fig. 1c). We temporally normalized individual CPP estimates to a condition-specific baseline during the final 250 ms preceding probe onset. As a proxy of evidence drift rate, CPP slopes were estimates via linear regression from -250 ms to -100 ms surrounding response execution, while the average CPP amplitude from -50 ms to 50 ms served as an indicator of decision thresholds (i.e., boundary separation; e.g., [152]).

Contralateral mu-beta. Decreases in contralateral mu-beta power provide a complementary, effector-specific signature of evidence integration [47,152]. We estimated mu-beta power using 7-cycle wavelets for the 8-25 Hz range with a step size of 50 ms. Spectral power was time-locked to probe presentation and response execution. We re-mapped channels to describe data recorded contra- and ipsi-lateral to the executed motor response in each trial, and averaged data from those channels to derive grand average mu-beta time courses. Individual average mu-beta time series were baseline-corrected using the -400 to -200 ms prior to probe onset, separately for each condition. For contralateral motor responses, remapped sites C3/5 and CP3/CP5 were selected based on the grand average topography for lateralized response executions (see inset in Figure S2a). Mu-beta slopes were estimated via linear regression from -250 ms to -50 ms prior to response execution, while the average power from -50 ms to 50 ms indexed decision thresholds (e.g., [152]).

Electrophysiological indices of top-down modulation during sensation

Low-frequency alpha and theta power. We estimated low-frequency power via a 7-cycle wavelet transform (linearly spaced center frequencies; 1 Hz steps; 2 to 15 Hz). The step size of estimates was 50 ms, ranging from -1.5 s prior to cue onset to 3.5 s following stimulus offset. Estimates were log10-transformed at the single trial level [158], with no explicit baseline-correction.

Steady State Visual Evoked Potential (SSVEP). The SSVEP characterizes the phase-locked, entrained visual activity (here 30 Hz) during dynamic stimulus updates (e.g., [159]). These features differentiate it from induced broadband activity or muscle artefacts in similar frequency bands. We used these properties to normalize individual single-trial SSVEP responses prior to averaging: (a) we calculated an FFT for overlapping one second epochs with a step size of

100 ms (Hanning-based multitaper) and averaged them within each uncertainty condition; (b) spectrally normalized 30 Hz estimates by subtracting the average of estimates at 28 and 32 Hz, effectively removing broadband effects (i.e., aperiodic slopes), and; (c) we subtracted a temporal baseline -700 to -100 ms prior to stimulus onset. Linear uncertainty effects on SSVEPs were assessed by paired t-tests on linear uncertainty slope estimates across posterior channel averages.

Time-resolved sample entropy. Sample entropy [160] quantifies the irregularity of a time series of length N by assessing the conditional probability that two sequences of m consecutive data points will remain similar when another sample ($m+1$) is included in the sequence (for a visual example see Figure 1A in [130]). Sample entropy is defined as the inverse natural logarithm of this conditional similarity: The similarity criterion (r) defines the tolerance within which two points are considered similar and is defined relative to the standard deviation (~variance) of the signal (here set to r = .5). We set the sequence length m to 2, in line with previous applications [130]. An adapted version of sample entropy calculations implemented in the mMSE toolbox (available from https://github.com/LNDG/mMSE) was used [130,161,162], wherein entropy is estimated across discontinuous data segments to provide time-resolved estimates. The estimation of scale-wise entropy across trials allows for an estimation of coarse scale entropy also for short time-bins (i.e., without requiring long, continuous signals), while quickly converging with entropy estimates from continuous recordings [161]. To remove the influence of posterior-occipital low-frequency rhythms on entropy estimates, we notch-filtered the 8-15 Hz alpha band using 6th order Butterworth filter prior to the entropy calculation [130]. Time-resolved entropy estimates were calculated for 500 ms windows from -1 s pre-stimulus to 1.25 s post-probe with a step size of 150 ms. As entropy values are implicitly normalized by the variance in each time bin via the similarity criterion, no temporal baseline correction was applied.

Aperiodic (1/f) slopes. The aperiodic 1/f slope of neural recordings is closely related to the sample entropy of broadband signals [130] and has been suggested as a proxy for cortical excitation-inhibition balance [129]. Spectral estimates were computed by means of a Fast Fourier Transform (FFT) over the final 2.5 s of the presentation period (to exclude onset transients) for linearly spaced frequencies between 2 and 80 Hz (step size of 0.5 Hz; Hanning-tapered segments zero-padded to 20 s) and subsequently averaged. Spectral power was log10-transformed to render power values more normally distributed across participants. Power spectral density (PSD) slopes were estimated using the fooof toolbox (v1.0.0-dev) using default parameters [163].

Pupil diameter. Pupil diameter was recorded during the EEG session using EyeLink 1000 at a sampling rate of 1000 Hz and was analyzed using FieldTrip and custom-written MATLAB scripts. Blinks were automatically indicated by the EyeLink software (version 4.40). To increase the sensitivity to periods of partially occluded pupils or eye movements, the first derivative of eye-tracker-based vertical eye movements was calculated, z-standardized, and outliers >= 3 STD were removed. We additionally removed data within 150 ms preceding or following indicated outliers. Finally, missing data were linearly interpolated, and data were epoched to 3.5 s prior to stimulus onset to 1 s following stimulus offset. We quantified phasic arousal responses via the rate of change of pupil diameter traces as this measure (i) has higher temporal precision and (ii) has been more strongly associated with noradrenergic responses than the overall response [164]. We downsampled pupil time series to 100 Hz. For visualization, but not statistics, we smoothed pupil traces using a moving average median of 300 ms.

fMRI-based analyses

Preprocessing of functional MRI data. fMRI data were preprocessed with FSL 5 (RRID:SCR_002823) [165,166]. Preprocessing included motion correction using McFLIRT, smoothing (7mm) and high-pass filtering (.01 Hz) using an 8th order zero-phase Butterworth filter applied using MATLAB's filtfilt function. We registered individual functional runs to the individual, ANTs brain-extracted T2w images (6 DOF), to T1w images (6 DOF) and finally to 3mm standard space (ICBM 2009c MNI152 nonlinear symmetric) [167] using nonlinear transformations in ANTs 2.1.0 [168] (for one participant, no T2w image was acquired and 6 DOF transformation of BOLD data was preformed directly to the T1w structural scan). We then masked the functional data with the ICBM 2009c GM tissue prior (thresholded at a probability of 0.25), and detrended the functional images (up to a cubic trend) using SPM12's spm_detrend. We also used a series of extended preprocessing steps to further reduce potential non-neural artifacts [135,169]. Specifically, we examined data within-subject, within-run via spatial independent component analysis (ICA) as implemented in FSL-MELODIC [170]. Due to the high multiband data dimensionality in the absence of low-pass filtering, we constrained the solution to 30 components per participant. Noise components were identified according to several key criteria: a) Spiking (components dominated by abrupt time series spikes); b) Motion (prominent edge or "ringing" effects, sometimes [but not always] accompanied by large time series spikes); c) Susceptibility and flow artifacts (prominent air-tissue boundary or sinus activation; typically represents cardio/respiratory effects); d) White matter (WM) and ventricle activation [171]; e) Low-frequency signal drift [172]; f) High power in high-frequency ranges unlikely to represent neural activity ($\geq$ 75% of total spectral power present above .10 Hz;); and g) Spatial distribution ("spotty" or "speckled" spatial pattern that appears scattered randomly across $\geq$ 25% of the brain, with few if any clusters with $\geq$ 80 contiguous voxels). Examples of these various components we typically deem to be noise can be found in [173]. By default, we utilized a conservative set of rejection criteria; if manual classification decisions were challenging due to mixing of "signal" and "noise" in a single component, we generally elected to keep such components. Three independent raters of noise components were utilized; > 90% inter-rater reliability was required on separate data before denoising decisions were made on the current data. Components identified as artifacts were then regressed from corresponding fMRI runs using the regfilt command in FSL. To reduce the influence of motion and physiological fluctuations, we regressed FSL's 6 DOF motion parameters from the data, in addition to average signal within white matter and CSF masks. Masks were created using 95% tissue probability thresholds to create conservative masks. Data and regressors were demeaned and linearly detrended prior to multiple linear regression for each run. To further reduce the impact of potential motion outliers, we censored significant DVARS outliers during the regression as described by [174]. We calculated the 'practical significance' of DVARS estimates and applied a threshold of 5 [175]. The regression-based residuals were subsequently spectrally interpolated during DVARS outliers as described in [174] and [176]. BOLD analyses were restricted to participants with both EEG and MRI data available (N = 42 YA, N = 53 OA).

fMRI decoding of prevalent feature options. We performed a decoding analysis to probe the extent to which participants' visual cortices contained information about the prevalent option of each feature. N = 2 older adults with two missing runs each were not included in this analysis due to the limited number of eligible trials. We trained a decoder based on BOLD signals from within a visual cortex mask that included Jülich parcellations ranging from V1 to area MT. We resliced the mask to 3mm and created an intersection mask with the cortical grey matter mask used throughout the remaining analyses. For classification analyses, we used linear support-vector machines (SVM) [177] implemented with libsvm (www.csie.ntu.edu.tw/~cjlin/libsvm). As no separate session was recorded, we trained classifiers based on all trials (across uncertainty conditions) for which the target feature was probed, therefore necessitating but not exhaustively capturing trials on which the respective feature was also cued. By experimental design, the number of trials during which a target feature was probed was matched across uncertainty levels. We used a bootstrap classification approach in the context of leave-one-out cross-validation to derive single-trial estimates of decoding accuracy. To increase the signal-to-noise ratio for the decoders, we averaged randomly selected trials into three folds (excluding any trial used for testing) and concatenated two pseudo-trials from each condition to create the training set. Trained decoders were then applied to the left-out trial. This train-and-test procedure was randomly repeated 100 times to create bootstrapped single-trial estimates. Finally, decoding accuracy was averaged across trials based on condition assignment (e.g., whether a given feature was cued or uncued). To assess above-chance decoding accuracy in time, we used univariate cluster-based permutation analyses (CBPAs). These univariate tests were performed by means of dependent samples t-tests, and cluster-based permutation tests [178] were performed to control for multiple comparisons. Initially, a clustering algorithm formed clusters based on significant t-tests of individual data points ($p <.05$, two-sided; cluster entry threshold) with the spatial constraint of a cluster covering a minimum of three neighboring channels. Then, the significance of the observed cluster-level statistic (based on the summed t-values within the cluster) was assessed by comparison to the distribution of all permutation-based cluster-level statistics. The final cluster p-value was assessed as the proportion of 1000 Monte Carlo iterations in which the cluster-level statistic was exceeded. Cluster significance was indicated by p-values below .025 (two-sided cluster significance threshold). To test uncertainty and age effects, we initially fitted linear mixed effects models with random intercepts and fixed effects of uncertainty, age, and an uncertainty x age interaction. As no significant interaction was indicated for any of the models (probed: $p = 0.760$; unprobed: $p = 0.434$; all: $p = 0.625$), we removed the interaction term for the main effect estimation. We constrained analysis to timepoints for which the cluster-based permutation analysis indicated above-chance decoding for cued features. We focused on probed and unprobed feature trials, as they are matched in trial number at each uncertainty level.

BOLD modulation by uncertainty and relation to external variables. We conducted a 1st level analysis using SPM12 to identify beta weights for each condition separately. Design variables included stimulus presentation (4 volumes; separate regressors for each uncertainty condition; parametrically modulated by sequence position), onset cue (no mod.), and probe (2 volumes, parametric modulation by RT). Design variables were convolved with a canonical HRF, including its temporal derivative as a nuisance term. Nuisance regressors included 24 motion parameters [179], as well as continuous DVARS estimates. Autoregressive modelling was implemented via FAST. Output beta images for each uncertainty condition were finally averaged across runs. We investigated the multivariate modulation of the BOLD response at the 2nd level using PLS analyses (see *Multivariate partial least squares analyses*). Specifically, we probed the relationship between voxel-wise 1st level beta weights and uncertainty within a task PLS. Next, we assessed the relationship between task-related BOLD signal changes and interindividual differences in the joint modulation of decision processes, cortical excitability, and pupil modulation by means of a behavioral PLS. For this, we first calculated linear slope coefficients for voxel-wise beta estimates. Then, we included the behavioral variables reported on the left of Figure 6c. For visualization, spatial clusters were defined based on a minimum distance of 10 mm, and by exceeding a size of 25 voxels. We identified regions associated with peak activity based on cytoarchitectonic probabilistic maps implemented in the SPM Anatomy Toolbox (Version 2.2c) [180]. If no assignment was found, the most proximal assignment to the peak coordinates was reported.

Temporal dynamics of thalamic engagement. To visualize the uncertainty modulation of thalamic activity, we extracted signals within a binary mask of thalamic divisions extracted from the Morel atlas [181]. Preprocessed BOLD timeseries were segmented into trials, spanning the period from the stimulus onset to the onset of the feedback phase. Given a time-to-peak of a canonical hemodynamic response function (HRF) between 5-6 seconds, we designated the 3 second interval from 5-8 seconds following the stimulus onset trigger as the stimulus presentation interval, and the 2 second interval from 3-5 s as the fixation interval, respectively. Single-trial time series were then temporally normalized to the temporal average during the approximate fixation interval.

Thalamic loci of behavioral PLS. To assess the thalamic loci of most reliable behavioral relations, we assessed bootstrap ratios within two thalamic masks. First, for nucleic subdivisions, we used the Morel parcellation scheme as consolidated and kindly provided by Hwang et al. [182] for 3 mm data at 3T field strength. The abbreviations are as follows: AN: anterior nucleus; VM: ventromedial; VL: ventrolateral; MGN: medial geniculate nucleus; LGN: lateral geniculate nucleus; MD: mediodorsal; PuA: anterior pulvinar; LP: lateral-posterior; IL: intra-laminar; VA: ventral-anterior; PuM: medial pulvinar; Pul: pulvinar proper; PuL: lateral pulvinar. Second, to assess cortical white-matter projections we considered the overlap with seven structurally derived cortical projection zones suggested by Horn & Blankenburg [183], which were derived from a large adult sample ($N = 169$). We binarized continuous probability maps at a relative 75% threshold of the respective maximum probability, and re-sliced masks to 3mm (ICBM 2009c MNI152).

Statistical analyses

Outlier handling. For each signature, we defined outliers at the subject-level as individuals within their respective age group whose values (e.g., estimates of linear modulation) exceeded three scaled median absolute deviations (MAD) as implemented in MATLAB. Such individual data points were winsorized prior to statistical analysis. For repeated measures analyses, such individuals were removed prior to statistical assessment.

Linear uncertainty effect estimates. To estimate the linear uncertainty modulation of dependent variables, we calculated 1st level beta estimates ($y = \text{intercept} + \beta * \text{target load} + e$) and assessed the slope difference from zero at the within-group level (see Table S1) using two-sided paired t-tests. Similarly, we compared linear uncertainty effect estimates between groups using two-sides unpaired t-tests. We assessed the relation of individual linear load effects between measures of interest via Pearson correlations.

Within-subject centering. To visually emphasize effects within participants, we use within-subject centering across repeated measures conditions by subtracting individual cross-condition means and adding global group means. For these visualizations, only the mean of the dependent values directly reflects the original units of measurement, as individual data points by construction do not reflect between-subject variation averaged across conditions. This procedure equals the creation of within-subject standard errors [184]. Within-subject centering is exclusively used for display and explicitly noted in the respective legends.

Multivariate partial least squares analyses. For data with a high-dimensional structure, we performed multivariate partial least squares analyses [185,186]. To assess main effect of probe uncertainty, we performed Task PLS analyses. Task PLS begins by calculating a between-subject covariance matrix (COV) between conditions and each neural value (e.g., time-space-frequency power), which is then decomposed using singular value decomposition (SVD). This yields a left singular vector of experimental condition weights (U), a right singular vector of brain weights (V), and a diagonal matrix of singular values (S). Task PLS produces orthogonal latent variables (LVs) that reflect optimal relations between experimental conditions and the neural data. We ran a version of task PLS in which group means were removed from condition means to highlight how conditions were modulated by group membership, i.e., condition and condition-by-group effects. To examine multivariate relations between neural data and other variables of interest, we performed behavioral PLS analyses. This analysis initially calculates a between-subject correlation matrix (CORR) between (1) each brain index of interest (e.g., 1st level BOLD beta values) and (2) a second 'behavioral' variable of interest (note that although called behavioral, this variable can reflect any variable of interest, e.g., behavior, pupil diameter, spectral power). CORR is then decomposed using singular value decomposition (SVD): $SVD_{CORR} = USV'$, which produces a matrix of left singular vectors of cognition weights (U), a matrix of right singular vectors of brain weights (V), and a diagonal matrix of singular values (S). For each LV (ordered strongest to weakest in S), a data pattern results which depicts the strongest available relation between brain data and other variables of interest. Significance of detected relations of both PLS model types was assessed using 1000 permutation tests of the singular value corresponding to the LV. A subsequent bootstrapping procedure indicated the robustness of within-LV neural saliences across 1000 resamples of the data [187]. By dividing each brain weight (from V) by its bootstrapped standard error, we obtained "bootstrap ratios" (BSRs) as normalized robustness estimates. We generally thresholded BSRs at values of ±3.00 (~99.9% confidence interval). We also obtained a summary measure of each participant's robust expression of a particular LV's pattern (a within-person "brain score") by multiplying the vector of brain weights (V) from each LV by each participant's vector of neural values (P), producing a single within-subject value: Brain score = VP'.

Data and code availability. Experiment code is available from https://git.mpib-berlin.mpg.de/LNDG/multi-attribute-task. Analysis code, primary EEG, fMRI, and behavioral data will be made available upon publication (for younger adults see https://osf.io/ug4b8/). Structural MRI data are exempt from public sharing according to obtained informed consent. All data are available from the corresponding authors upon reasonable request**.**

Acknowledgements. This study was conducted within the 'Lifespan Neural Dynamics Group' at the Max Planck UCL Centre for Computational Psychiatry and Ageing Research in the Max Planck Institute for Human Development (MPIB) in Berlin, Germany. DDG was supported by an Emmy Noether Programme grant from the German Research Foundation. UL acknowledges financial support from the Intramural Innovation Fund of the Max Planck Society. JQK, DDG and UL were partially supported by the Max Planck UCL Centre for Computational Psychiatry and Ageing Research. The participating institutions are the Max Planck Institute for Human Development, Berlin, Germany, and University College London, London, UK. For more information, see https://www.mps-ucl-centre.mpg.de/en/comp2psych. The funders had no role in study design, data collection and analysis, decision to publish, or preparation of the manuscript. We thank our research assistants and participants for their contributions to the present work.

Author contributions. JQK: Conceptualization, Methodology, Investigation, Software, Formal analysis, Visualization, Writing – original draft, Writing – review and editing, Validation, Data Curation; UM: Conceptualization, Writing – review and editing, UL: Conceptualization, Resources, Writing – review and editing, Supervision, Funding acquisition; DDG: Conceptualization, Methodology, Software, Resources, Writing—review and editing, Supervision, Project administration, Funding acquisition.

Competing interests. The authors declare no competing interests.

References

1. Desimone, R. & Duncan, J. Neural Mechanisms of Selective Visual-Attention. *Annual Review of Neuroscience* **18**, 193-222 (1995).
2. Findling, C., Skvortsova, V., Dromnelle, R., Palminteri, S. & Wyart, V. Computational noise in reward-guided learning drives behavioral variability in volatile environments. *Nat Neurosci* **22**, 2066-2077 (2019).
3. Tavoni, G., Doi, T., Pizzica, C., Balasubramanian, V. & Gold, J. I. Human inference reflects a normative balance of complexity and accuracy. *Nat Hum Behav* **6**, 1153-1168 (2022).
4. Huys, Q. J. M., Browning, M., Paulus, M. P. & Frank, M. J. Advances in the computational understanding of mental illness. *Neuropsychopharmacology* **46**, 3-19 (2021).
5. Pulcu, E. & Browning, M. The Misestimation of Uncertainty in Affective Disorders. *Trends in cognitive sciences* **23**, 865-875 (2019).
6. Quigley, C. & Muller, M. M. Feature-selective attention in healthy old age: a selective decline in selective attention? *The Journal of neuroscience : the official journal of the Society for Neuroscience* **34**, 2471-2476 (2014).
7. Amer, T. & Hasher, L. Conceptual processing of distractors by older but not younger adults. *Psychol Sci* **25**, 2252-2258 (2014).
8. Kennedy, B. L. & Mather, M. in *The aging brain: Functional adaptation across adulthood* (ed G. R. Samanez-Larkin) 45–72 (American Psychological Association, 2019).
9. Hasher, L. & Zacks, R. T. in *The psychology of learning and motivation* Vol. 22 (ed G. H. Bower) pp. 193-225 (Academic Press, 1988).
10. Salthouse, T. A. & Meinz, E. J. Aging, Inhibition, Working-Memory, and Speed. *J Gerontol B-Psychol* **50**, P297-P306 (1995).
11. Lindenberger, U. & Mayr, U. Cognitive aging: is there a dark side to environmental support? *Trends in cognitive sciences* **18**, 7-15 (2014).
12. McDowd, J. M. & Craik, F. I. M. Effects of aging and task difficulty on divided attention performance. *Journal of experimental psychology. Human perception and performance* **14**, 267-280 (1988).
13. Kray, J., Li, K. Z. & Lindenberger, U. Age-related changes in task-switching components: the role of task uncertainty. *Brain and cognition* **49**, 363-381 (2002).
14. Mayr, U. Age differences in the selection of mental sets: the role of inhibition, stimulus ambiguity, and response-set overlap. *Psychology and aging* **16**, 96-109 (2001).
15. Spieler, D. H., Mayr, U. & LaGrone, S. Outsourcing cognitive control to the environment: adult age differences in the use of task cues. *Psychon Bull Rev* **13**, 787-793 (2006).
16. Nassar, M. R. *et al.* Age differences in learning emerge from an insufficient representation of uncertainty in older adults. *Nat Commun* **7**, 11609 (2016).
17. Bach, D. R. & Dolan, R. J. Knowing how much you don't know: a neural organization of uncertainty estimates. *Nature reviews. Neuroscience* **13**, 572-586 (2012).
18. Xue, C., Kramer, L. E. & Cohen, M. R. Dynamic task-belief is an integral part of decision-making. *Neuron* **110** (2022).
19. Okazawa, G. & Kiani, R. Neural Mechanisms that Make Perceptual Decisions Flexible. *Annu Rev Physiol* (2022).
20. Mante, V., Sussillo, D., Shenoy, K. V. & Newsome, W. T. Context-dependent computation by recurrent dynamics in prefrontal cortex. *Nature* **503**, 78-84 (2013).
21. Miller, E. K. & Buschman, T. J. Cortical circuits for the control of attention. *Current Opinion in Neurobiology* **23**, 216-222 (2013).
22. Halassa, M. M. & Kastner, S. Thalamic functions in distributed cognitive control. *Nat Neurosci* **20**, 1669-1679 (2017).
23. Rikhye, R. V., Gilra, A. & Halassa, M. M. Thalamic regulation of switching between cortical representations enables cognitive flexibility. *Nat Neurosci* **21**, 1753-1763 (2018).
24. Moher, J., Lakshmanan, B. M., Egeth, H. E. & Ewen, J. B. Inhibition drives early feature-based attention. *Psychol Sci* **25**, 315-324 (2014).
25. Jehee, J. F., Brady, D. K. & Tong, F. Attention improves encoding of task-relevant features in the human visual cortex. *The Journal of neuroscience : the official journal of the Society for Neuroscience* **31**, 8210-8219 (2011).
26. Griffiths, B. J. *et al.* Alpha/beta power decreases track the fidelity of stimulus-specific information. *Elife* **8**, 633107 (2019).
27. Kosciessa, J. Q., Lindenberger, U. & Garrett, D. D. Thalamocortical excitability modulation guides human perception under uncertainty. *Nat Commun* **12**, 2430 (2021).
28. Joshi, S., Li, Y., Kalwani, R. M. & Gold, J. I. Relationships between Pupil Diameter and Neuronal Activity in the Locus Coeruleus, Colliculi, and Cingulate Cortex. *Neuron* **89**, 221-234 (2016).
29. Nyberg, L. *et al.* Longitudinal evidence for diminished frontal cortex function in aging. *Proceedings of the National Academy of Sciences of the United States of America* **107**, 22682-22686 (2010).
30. Pardo, J. V. *et al.* Where the brain grows old: decline in anterior cingulate and medial prefrontal function with normal aging. *Neuroimage* **35**, 1231-1237 (2007).
31. Ishibashi, K. *et al.* Longitudinal effects of aging on (18)F-FDG distribution in cognitively normal elderly individuals. *Sci Rep-Uk* **8**, 11557 (2018).
32. Pardo, J. V., Nyabwari, S. M., Lee, J. T. & Alzheimer's Disease Neuroimaging, I. Aging-Related Hypometabolism in the Anterior Cingulate Cortex of Cognitively Intact, Amyloid-Negative Seniors at Rest Mediates the Relationship between Age and Executive Function but Not Memory. *Cereb Cortex Commun* **1**, tgaa020 (2020).
33. Li, S. C., Lindenberger, U. & Sikstrom, S. Aging cognition: from neuromodulation to representation. *Trends in cognitive sciences* **5**, 479-486 (2001).
34. Backman, L., Lindenberger, U., Li, S. C. & Nyberg, L. Linking cognitive aging to alterations in dopamine neurotransmitter functioning: recent data and future avenues. *Neuroscience and biobehavioral reviews* **34**, 670-677 (2010).

35 Mather, M. & Harley, C. W. The Locus Coeruleus: Essential for Maintaining Cognitive Function and the Aging Brain. *Trends in cognitive sciences* **20**, 214-226 (2016).

36 Lalwani, P. *et al.* Neural distinctiveness declines with age in auditory cortex and is associated with auditory GABA levels. *Neuroimage* **201** (2019).

37 Simmonite, M. *et al.* Age-Related Declines in Occipital GABA are Associated with Reduced Fluid Processing Ability. *Acad Radiol* **26**, 1053-1061 (2019).

38 Fama, R. & Sullivan, E. V. Thalamic structures and associated cognitive functions: Relations with age and aging. *Neuroscience and biobehavioral reviews* **54**, 29-37 (2015).

39 Garrett, D. D. *et al.* Lost Dynamics and the Dynamics of Loss: Longitudinal Compression of Brain Signal Variability is Coupled with Declines in Functional Integration and Cognitive Performance. *Cereb Cortex* **31**, 5239-5252 (2021).

40 Cabeza, R. *et al.* Maintenance, reserve and compensation: the cognitive neuroscience of healthy ageing. *Nature reviews. Neuroscience* **19**, 701-710 (2018).

41 Nagel, I. E. *et al.* Performance level modulates adult age differences in brain activation during spatial working memory. *Proceedings of the National Academy of Sciences of the United States of America* **106**, 22552-22557 (2009).

42 Garrett, D. D., Kovacevic, N., McIntosh, A. R. & Grady, C. L. The modulation of BOLD variability between cognitive states varies by age and processing speed. *Cereb Cortex* **23**, 684-693 (2013).

43 Dias, R., Robbins, T. W. & Roberts, A. C. Dissociation in prefrontal cortex of affective and attentional shifts. *Nature* **380**, 69-72 (1996).

44 Friedman, N. P. & Robbins, T. W. The role of prefrontal cortex in cognitive control and executive function. *Neuropsychopharmacology* **47**, 72-89 (2022).

45 Wiecki, T. V., Sofer, I. & Frank, M. J. HDDM: Hierarchical Bayesian estimation of the Drift-Diffusion Model in Python. *Front Neuroinform* **7**, 14 (2013).

46 Kelly, S. P. & O'Connell, R. G. Internal and external influences on the rate of sensory evidence accumulation in the human brain. *The Journal of neuroscience : the official journal of the Society for Neuroscience* **33**, 19434-19441 (2013).

47 Donner, T. H., Siegel, M., Fries, P. & Engel, A. K. Buildup of choice-predictive activity in human motor cortex during perceptual decision making. *Current biology : CB* **19**, 1581-1585 (2009).

48 Cohen, J. D., Dunbar, K. & McClelland, J. L. On the control of automatic processes: a parallel distributed processing account of the Stroop effect. *Psychological review* **97**, 332-361 (1990).

49 Davidson, D. J., Zacks, R. T. & Williams, C. C. Stroop interference, practice, and aging. *Neuropsychology, development, and cognition. Section B, Aging, neuropsychology and cognition* **10**, 85-98 (2003).

50 Cavanagh, J. F. & Frank, M. J. Frontal theta as a mechanism for cognitive control. *Trends in cognitive sciences* **18**, 414-421 (2014).

51 Cavanagh, J. F., Figueroa, C. M., Cohen, M. X. & Frank, M. J. Frontal Theta Reflects Uncertainty and Unexpectedness during Exploration and Exploitation. *Cerebral Cortex* **22**, 2575-2586 (2012).

52 McGinley, M. J. *et al.* Waking State: Rapid Variations Modulate Neural and Behavioral Responses. *Neuron* **87**, 1143-1161 (2015).

53 Thiele, A. & Bellgrove, M. A. Neuromodulation of Attention. *Neuron* **97**, 769-785 (2018).

54 Gompf, H. S. *et al.* Locus ceruleus and anterior cingulate cortex sustain wakefulness in a novel environment. *The Journal of neuroscience : the official journal of the Society for Neuroscience* **30**, 14543-14551 (2010).

55 Muller, T. H., Mars, R. B., Behrens, T. E. & O'Reilly, J. X. Control of entropy in neural models of environmental state. *Elife* **8** (2019).

56 Critchley, H. D., Tang, J., Glaser, D., Butterworth, B. & Dolan, R. J. Anterior cingulate activity during error and autonomic response. *Neuroimage* **27**, 885-895 (2005).

57 Joshi, S. & Gold, J. I. Pupil Size as a Window on Neural Substrates of Cognition. *Trends in cognitive sciences* **24**, 466-480 (2020).

58 Nassar, M. R. *et al.* Rational regulation of learning dynamics by pupil-linked arousal systems. *Nat Neurosci* **15**, 1040-1046 (2012).

59 Murphy, P. R., Wilming, N., Hernandez-Bocanegra, D. C., Prat-Ortega, G. & Donner, T. H. Adaptive circuit dynamics across human cortex during evidence accumulation in changing environments. *Nat Neurosci* **24**, 987-997 (2021).

60 Weber, J. *et al.* Population coding and oscillatory subspace synchronization integrate context into actions. *bioRxiv*, 2021.2012.2017.473118 (2021).

61 Mukherjee, A., Lam, N. H., Wimmer, R. D. & Halassa, M. M. Thalamic circuits for independent control of prefrontal signal and noise. *Nature* (2021).

62 Soltani, A. & Izquierdo, A. Adaptive learning under expected and unexpected uncertainty. *Nature Reviews Neuroscience* **20**, 635-644 (2019).

63 Nyberg, L., Lovden, M., Riklund, K., Lindenberger, U. & Backman, L. Memory aging and brain maintenance. *Trends in cognitive sciences* **16**, 292-305 (2012).

64 Ridderinkhof, K. R., Ullsperger, M., Crone, E. A. & Nieuwenhuis, S. The role of the medial frontal cortex in cognitive control. *Science* **306**, 443-447 (2004).

65 Enel, P., Procyk, E., Quilodran, R. & Dominey, P. F. Reservoir Computing Properties of Neural Dynamics in Prefrontal Cortex. *Plos Comput Biol* **12**, e1004967 (2016).

66 Holroyd, C. B., Ribas-Fernandes, J. J. F., Shahnazian, D., Silvetti, M. & Verguts, T. Human midcingulate cortex encodes distributed representations of task progress. *Proceedings of the National Academy of Sciences of the United States of America* **115**, 6398-6403 (2018).

67 Lapish, C. C., Durstewitz, D., Chandler, L. J. & Seamans, J. K. Successful choice behavior is associated with distinct and coherent network states in anterior cingulate cortex. *Proceedings of the National Academy of Sciences of the United States of America* **105**, 11963-11968 (2008).

68 Behrens, T. E., Woolrich, M. W., Walton, M. E. & Rushworth, M. F. Learning the value of information in an uncertain world. *Nat Neurosci* **10**, 1214-1221 (2007).

69 Geurts, L. S., Cooke, J. R. H., van Bergen, R. S. & Jehee, J. F. M. Subjective confidence reflects representation of Bayesian probability in cortex. *Nat Hum Behav* **6**, 294-305 (2022).

70 Powell, N. J. & Redish, A. D. Representational changes of latent strategies in rat medial prefrontal cortex precede changes in behaviour. *Nat Commun* **7**, 12830 (2016).

71 Minxha, J., Adolphs, R., Fusi, S., Mamelak, A. N. & Rutishauser, U. Flexible recruitment of memory-based choice representations by the human medial frontal cortex. *Science* **368** (2020).

72 White, J. K. *et al.* A neural network for information seeking. *Nat Commun* **10**, 5168 (2019).

73 Domenech, P., Rheims, S. & Koechlin, E. Neural mechanisms resolving exploitation-exploration dilemmas in the medial prefrontal cortex. *Science* **369** (2020).

74 Karlsson, M. P., Tervo, D. G. & Karpova, A. Y. Network resets in medial prefrontal cortex mark the onset of behavioral uncertainty. *Science* **338**, 135-139 (2012).

75 Buschman, T. J., Denovellis, E. L., Diogo, C., Bullock, D. & Miller, E. K. Synchronous Oscillatory Neural Ensembles for Rules in the Prefrontal Cortex. *Neuron* **76**, 838-846 (2012).

76 Schuck, N. W. *et al.* Medial prefrontal cortex predicts internally driven strategy shifts. *Neuron* **86**, 331-340 (2015).

77 Holroyd, C. B. & Verguts, T. The Best Laid Plans: Computational Principles of Anterior Cingulate Cortex. *Trends in cognitive sciences* **25**, 316-329 (2021).

78 Monosov, I. E., Haber, S. N., Leuthardt, E. C. & Jezzini, A. Anterior Cingulate Cortex and the Control of Dynamic Behavior in Primates. *Current biology : CB* **30**, R1442-R1454 (2020).

79 Schmitt, L. I. *et al.* Thalamic amplification of cortical connectivity sustains attentional control. *Nature* **545**, 219-223 (2017).

80 Bolkan, S. S. *et al.* Thalamic projections sustain prefrontal activity during working memory maintenance (vol 20, pg 987, 2017). *Nature Neuroscience* **21**, 1138-1138 (2018).

81 Trick, L. M., Perl, T. & Sethi, N. Age-related differences in multiple-object tracking. *J Gerontol B-Psychol* **60**, P102-P105 (2005).

82 Dorum, E. S. *et al.* Age-related differences in brain network activation and co-activation during multiple object tracking. *Brain Behav* **6** (2016).

83 Wild-Wall, N. & Falkenstein, M. Age-dependent impairment of auditory processing under spatially focused and divided attention: An electrophysiological study. *Biological Psychology* **83**, 27-36 (2010).

84 Ueltzhoffer, K., Armbruster-Genc, D. J. & Fiebach, C. J. Stochastic Dynamics Underlying Cognitive Stability and Flexibility. *Plos Comput Biol* **11**, e1004331 (2015).

85 Cummins, T. D. R. & Finnigan, S. Theta power is reduced in healthy cognitive aging. *Int J Psychophysiol* **66**, 10-17 (2007).

86 Anguera, J. A. *et al.* Video game training enhances cognitive control in older adults. *Nature* **501**, 97-101 (2013).

87 Arenaza-Urquijo, E. M. *et al.* Relationships between years of education and gray matter volume, metabolism and functional connectivity in healthy elders. *Neuroimage* **83**, 450-457 (2013).

88 Aston-Jones, G. & Cohen, J. D. An integrative theory of locus coeruleus-norepinephrine function: adaptive gain and optimal performance. *Annu Rev Neurosci* **28**, 403-450 (2005).

89 Yu, A. J. & Dayan, P. Uncertainty, neuromodulation, and attention. *Neuron* **46**, 681-692 (2005).

90 Carter, M. E. *et al.* Tuning arousal with optogenetic modulation of locus coeruleus neurons. *Nat Neurosci* **13**, 1526-1533 (2010).

91 Geng, J. J., Blumenfeld, Z., Tyson, T. L. & Minzenberg, M. J. Pupil diameter reflects uncertainty in attentional selection during visual search. *Frontiers in human neuroscience* **9**, 435 (2015).

92 Jepma, M. & Nieuwenhuis, S. Pupil diameter predicts changes in the exploration-exploitation trade-off: evidence for the adaptive gain theory. *Journal of cognitive neuroscience* **23**, 1587-1596 (2011).

93 Vincent, P., Parr, T., Benrimoh, D. & Friston, K. J. With an eye on uncertainty: Modelling pupillary responses to environmental volatility. *Plos Comput Biol* **15**, e1007126 (2019).

94 Hammerer, D. *et al.* Locus coeruleus integrity in old age is selectively related to memories linked with salient negative events. *Proceedings of the National Academy of Sciences of the United States of America* **115**, 2228-2233 (2018).

95 Dahl, M. J., Mather, M., Sander, M. C. & Werkle-Bergner, M. Noradrenergic Responsiveness Supports Selective Attention across the Adult Lifespan. *The Journal of neuroscience : the official journal of the Society for Neuroscience* **40**, 4372-4390 (2020).

96 Arnsten, A. F. T. & Goldmanrakic, P. S. Catecholamines and Cognitive Decline in Aged Nonhuman-Primates. *Annals of the New York Academy of Sciences* **444**, 218-234 (1985).

97 Ebitz, R. B. & Platt, M. L. Neuronal activity in primate dorsal anterior cingulate cortex signals task conflict and predicts adjustments in pupil-linked arousal. *Neuron* **85**, 628-640 (2015).

98 Froemke, R. C. Plasticity of cortical excitatory-inhibitory balance. *Annu Rev Neurosci* **38**, 195-219 (2015).

99 Munn, B. R., Muller, E. J., Wainstein, G. & Shine, J. M. The ascending arousal system shapes neural dynamics to mediate awareness of cognitive states. *Nat Commun* **12**, 6016 (2021).

100 De Martino, B., Fleming, S. M., Garrett, N. & Dolan, R. J. Confidence in value-based choice. *Nat Neurosci* **16**, 105-110 (2013).

101 McGuire, J. T., Nassar, M. R., Gold, J. I. & Kable, J. W. Functionally dissociable influences on learning rate in a dynamic environment. *Neuron* **84**, 870-881 (2014).

102 Li, S. C. & Rieckmann, A. Neuromodulation and aging: implications of aging neuronal gain control on cognition. *Current Opinion in Neurobiology* **29**, 148-158 (2014).

103 Backman, L., Nyberg, L., Lindenberger, U., Li, S. C. & Farde, L. The correlative triad among aging, dopamine, and cognition: Current status and future prospects. *Neuroscience and biobehavioral reviews* **30**, 791-807 (2006).

104 Durstewitz, D. & Seamans, J. K. The dual-state theory of prefrontal cortex dopamine function with relevance to catechol-o-methyltransferase genotypes and schizophrenia. *Biol Psychiatry* **64**, 739-749 (2008).
105 Rolls, E. T., Loh, M., Deco, G. & Winterer, G. Computational models of schizophrenia and dopamine modulation in the prefrontal cortex. *Nature reviews. Neuroscience* **9**, 696-709 (2008).
106 Lapish, C. C., Balaguer-Ballester, E., Seamans, J. K., Phillips, A. G. & Durstewitz, D. Amphetamine Exerts Dose-Dependent Changes in Prefrontal Cortex Attractor Dynamics during Working Memory. *The Journal of neuroscience : the official journal of the Society for Neuroscience* **35**, 10172-10187 (2015).
107 Hashemnia, S., Euston, D. R. & Gruber, A. J. Amphetamine reduces reward encoding and stabilizes neural dynamics in rat anterior cingulate cortex. *Elife* **9** (2020).
108 Samanez-Larkin, G. R. *et al.* A thalamocorticostriatal dopamine network for psychostimulant-enhanced human cognitive flexibility. *Biol Psychiatry* **74**, 99-105 (2013).
109 Garrett, D. D. *et al.* Dynamic regulation of neural variability during working memory reflects dopamine, functional integration, and decision-making. *bioRxiv*, 2022.2005.2005.490687 (2022).
110 Ma, W. J., Husain, M. & Bays, P. M. Changing concepts of working memory. *Nat Neurosci* **17**, 347-356 (2014).
111 Klimesch, W., Sauseng, P. & Hanslmayr, S. EEG alpha oscillations: the inhibition-timing hypothesis. *Brain Res Rev* **53**, 63-88 (2007).
112 Haegens, S., Nacher, V., Luna, R., Romo, R. & Jensen, O. alpha-Oscillations in the monkey sensorimotor network influence discrimination performance by rhythmical inhibition of neuronal spiking. *Proceedings of the National Academy of Sciences of the United States of America* **108**, 19377-19382 (2011).
113 Capilla, A., Schoffelen, J. M., Paterson, G., Thut, G. & Gross, J. Dissociated alpha-Band Modulations in the Dorsal and Ventral Visual Pathways in Visuospatial Attention and Perception. *Cerebral Cortex* **24**, 550-561 (2014).
114 Jensen, O. & Mazaheri, A. Shaping functional architecture by oscillatory alpha activity: gating by inhibition. *Frontiers in human neuroscience* **4** (2010).
115 Sauseng, P. *et al.* Brain oscillatory substrates of visual short-term memory capacity. *Current biology : CB* **19**, 1846-1852 (2009).
116 Borghini, G. *et al.* Alpha Oscillations Are Causally Linked to Inhibitory Abilities in Ageing. *Journal of Neuroscience* **38**, 4418-4429 (2018).
117 ElShafei, H. A., Fornoni, L., Masson, R., Bertrand, O. & Bidet-Caulet, A. Age-related modulations of alpha and gamma brain activities underlying anticipation and distraction. *PloS one* **15** (2020).
118 Vaden, R. J., Hutcheson, N. L., McCollum, L. A., Kentros, J. & Visscher, K. M. Older adults, unlike younger adults, do not modulate alpha power to suppress irrelevant information. *Neuroimage* **63**, 1127-1133 (2012).
119 Leenders, M. P., Lozano-Soldevilla, D., Roberts, M. J., Jensen, O. & De Weerd, P. Diminished Alpha Lateralization During Working Memory but Not During Attentional Cueing in Older Adults. *Cereb Cortex* **28**, 21-32 (2018).
120 Lee, T. H. *et al.* Arousal increases neural gain via the locus coeruleus-norepinephrine system in younger adults but not in older adults. *Nat Hum Behav* **2**, 356-366 (2018).
121 Gazzaley, A. & D'Esposito, M. Top-down modulation and normal aging. *Annals of the New York Academy of Sciences* **1097**, 67-83 (2007).
122 Gazzaley, A. *et al.* Age-related top-down suppression deficit in the early stages of cortical visual memory processing. *Proceedings of the National Academy of Sciences of the United States of America* **105**, 13122-13126 (2008).
123 Klimesch, W. EEG alpha and theta oscillations reflect cognitive and memory performance: a review and analysis. *Brain Res Brain Res Rev* **29**, 169-195 (1999).
124 Borghini, G., Astolfi, L., Vecchiato, G., Mattia, D. & Babiloni, F. Measuring neurophysiological signals in aircraft pilots and car drivers for the assessment of mental workload, fatigue and drowsiness. *Neuroscience and biobehavioral reviews* **44**, 58-75 (2014).
125 Kardan, O. *et al.* Distinguishing cognitive effort and working memory load using scale-invariance and alpha suppression in EEG. *Neuroimage* **211** (2020).
126 Fukuda, K., Mance, I. & Vogel, E. K. alpha Power Modulation and Event-Related Slow Wave Provide Dissociable Correlates of Visual Working Memory. *The Journal of neuroscience : the official journal of the Society for Neuroscience* **35**, 14009-14016 (2015).
127 Zanto, T. P. & Gazzaley, A. Neural suppression of irrelevant information underlies optimal working memory performance. *The Journal of neuroscience : the official journal of the Society for Neuroscience* **29**, 3059-3066 (2009).
128 Sghirripa, S. *et al.* Load-dependent modulation of alpha oscillations during working memory encoding and retention in young and older adults. *Psychophysiology* **58** (2021).
129 Gao, R., Peterson, E. J. & Voytek, B. Inferring synaptic excitation/inhibition balance from field potentials. *Neuroimage* **158**, 70-78 (2017).
130 Kosciessa, J. Q., Kloosterman, N. A. & Garrett, D. D. Standard multiscale entropy reflects neural dynamics at mismatched temporal scales: What's signal irregularity got to do with it? *Plos Comput Biol* **16**, e1007885 (2020).
131 McIntosh, A. R. *et al.* Spatiotemporal Dependency of Age-Related Changes in Brain Signal Variability. *Cerebral Cortex* **24**, 1806-1817 (2014).
132 Voytek, B. *et al.* Age-Related Changes in 1/f Neural Electrophysiological Noise. *Journal of Neuroscience* **35**, 13257-13265 (2015).
133 Waschke, L., Wostmann, M. & Obleser, J. States and traits of neural irregularity in the age-varying human brain. *Scientific Reports* **7** (2017).
134 Waschke, L., Kloosterman, N. A., Obleser, J. & Garrett, D. D. Behavior needs neural variability. *Neuron* **109**, 751-766 (2021).
135 Garrett, D. D. *et al.* Amphetamine modulates brain signal variability and working memory in younger and older adults. *Proceedings of the National Academy of Sciences of the United States of America* **112**, 7593-7598 (2015).

136 Komura, Y., Nikkuni, A., Hirashima, N., Uetake, T. & Miyamoto, A. Responses of pulvinar neurons reflect a subject's confidence in visual categorization. *Nature Neuroscience* **16**, 749-755 (2013).

137 Jaramillo, J., Mejias, J. F. & Wang, X. J. Engagement of Pulvino-cortical Feedforward and Feedback Pathways in Cognitive Computations. *Neuron* **101**, 321-336 e329 (2019).

138 Wilke, M., Turchi, J., Smith, K., Mishkin, M. & Leopold, D. A. Pulvinar inactivation disrupts selection of movement plans. *The Journal of neuroscience : the official journal of the Society for Neuroscience* **30**, 8650-8659 (2010).

139 Oldfield, R. C. The assessment and analysis of handedness: the Edinburgh inventory. *Neuropsychologia* **9**, 97-113 (1971).

140 Folstein, M. F., Robins, L. N. & Helzer, J. E. The Mini-Mental State Examination. *Arch Gen Psychiat* **40**, 812-812 (1983).

141 Kessler, J., Markowitsch, H. & Denzler, P. *Mini-mental-status-test (MMST).* (Beltz Test GMBH, 2000).

142 Kleiner, M., Brainard, D. & Pelli, D. What's new in Psychtoolbox-3? *Perception* **36**, 14-14 (2007).

143 Pelli, D. G. The VideoToolbox software for visual psychophysics: Transforming numbers into movies. *Spatial Vision* **10**, 437-442 (1997).

144 Brainard, D. H. The Psychophysics Toolbox. *Spatial Vision* **10**, 433-436 (1997).

145 Oostenveld, R. & Praamstra, P. The five percent electrode system for high-resolution EEG and ERP measurements. *Clin Neurophysiol* **112**, 713-719 (2001).

146 Gold, J. I. & Shadlen, M. N. The neural basis of decision making. *Annu Rev Neurosci* **30**, 535-574 (2007).

147 Hanks, T. D. & Summerfield, C. Perceptual Decision Making in Rodents, Monkeys, and Humans. *Neuron* **93**, 15-31 (2017).

148 Siegel, M., Buschman, T. J. & Miller, E. K. Cortical information flow during flexible sensorimotor decisions. *Science* **348**, 1352-1355 (2015).

149 Banca, P. *et al.* Evidence accumulation in obsessive-compulsive disorder: the role of uncertainty and monetary reward on perceptual decision-making thresholds. *Neuropsychopharmacology* **40**, 1192-1202 (2015).

150 Ratcliff, R. Theory of Memory Retrieval. *Psychological review* **85**, 59-108 (1978).

151 Frank, M. J. *et al.* fMRI and EEG predictors of dynamic decision parameters during human reinforcement learning. *The Journal of neuroscience : the official journal of the Society for Neuroscience* **35**, 485-494 (2015).

152 McGovern, D. P., Hayes, A., Kelly, S. P. & O'Connell, R. G. Reconciling age-related changes in behavioural and neural indices of human perceptual decision-making. *Nat Hum Behav* **2**, 955-966 (2018).

153 Oostenveld, R., Fries, P., Maris, E. & Schoffelen, J. M. FieldTrip: Open source software for advanced analysis of MEG, EEG, and invasive electrophysiological data. *Computational intelligence and neuroscience* **2011**, 156869 (2011).

154 Bell, A. J. & Sejnowski, T. J. An information-maximization approach to blind separation and blind deconvolution. *Neural Comput* **7**, 1129-1159 (1995).

155 Nolan, H., Whelan, R. & Reilly, R. B. FASTER: Fully Automated Statistical Thresholding for EEG artifact Rejection. *Journal of neuroscience methods* **192**, 152-162 (2010).

156 Perrin, F., Pernier, J., Bertrand, O. & Echallier, J. F. Spherical splines for scalp potential and current density mapping. *Electroencephalography and clinical neurophysiology* **72**, 184-187 (1989).

157 O'Connell, R. G., Dockree, P. M. & Kelly, S. P. A supramodal accumulation-to-bound signal that determines perceptual decisions in humans. *Nat Neurosci* **15**, 1729-1735 (2012).

158 Smulders, F. T. Y., ten Oever, S., Donkers, F. C. L., Quaedflieg, C. W. E. M. & van de Ven, V. Single-trial log transformation is optimal in frequency analysis of resting EEG alpha. *European Journal of Neuroscience* **48**, 2585-2598 (2018).

159 Ding, J., Sperling, G. & Srinivasan, R. Attentional modulation of SSVEP power depends on the network tagged by the flicker frequency. *Cereb Cortex* **16**, 1016-1029 (2006).

160 Richman, J. S. & Moorman, J. R. Physiological time-series analysis using approximate entropy and sample entropy. *Am J Physiol-Heart C* **278**, H2039-H2049 (2000).

161 Grandy, T. H., Garrett, D. D., Schmiedek, F. & Werkle-Bergner, M. On the estimation of brain signal entropy from sparse neuroimaging data. *Sci Rep-Uk* **6**, 23073 (2016).

162 Kloosterman, N. A., Kosciessa, J. Q., Lindenberger, U., Fahrenfort, J. J. & Garrett, D. D. Boosts in brain signal variability track liberal shifts in decision bias. *Elife* **9** (2020).

163 Donoghue, T. *et al.* Parameterizing neural power spectra into periodic and aperiodic components. *Nat Neurosci* **23**, 1655-1665 (2020).

164 Reimer, J. *et al.* Pupil fluctuations track fast switching of cortical states during quiet wakefulness. *Neuron* **84**, 355-362 (2014).

165 Jenkinson, M., Beckmann, C. F., Behrens, T. E., Woolrich, M. W. & Smith, S. M. Fsl. *Neuroimage* **62**, 782-790 (2012).

166 Smith, S. M. *et al.* Advances in functional and structural MR image analysis and implementation as FSL. *Neuroimage* **23**, S208-S219 (2004).

167 Fonov, V. *et al.* Unbiased average age-appropriate atlases for pediatric studies. *Neuroimage* **54**, 313-327 (2011).

168 Avants, B. B. *et al.* A reproducible evaluation of ANTs similarity metric performance in brain image registration. *Neuroimage* **54**, 2033-2044 (2011).

169 Garrett, D. D., Kovacevic, N., McIntosh, A. R. & Grady, C. L. Blood oxygen level-dependent signal variability is more than just noise. *The Journal of neuroscience : the official journal of the Society for Neuroscience* **30**, 4914-4921 (2010).

170 Beckmann, C. F. & Smith, S. M. Probabilistic independent component analysis for functional magnetic resonance imaging. *Ieee T Med Imaging* **23**, 137-152 (2004).

171 Birn, R. M. The role of physiological noise in resting-state functional connectivity. *Neuroimage* **62**, 864-870 (2012).

172 Smith, A. M. *et al.* Investigation of low frequency drift in fMRI signal. *Neuroimage* **9**, 526-533 (1999).

173 Garrett, D. D., McIntosh, A. R. & Grady, C. L. Brain signal variability is parametrically modifiable. *Cereb Cortex* **24**, 2931-2940 (2014).

174 Power, J. D. *et al.* Methods to detect, characterize, and remove motion artifact in resting state fMRI. *Neuroimage* **84**, 320-341 (2014).

175 Afyouni, S. & Nichols, T. E. Insight and inference for DVARS. *Neuroimage* **172**, 291-312 (2018).

176 Parkes, L., Fulcher, B., Yucel, M. & Fornito, A. An evaluation of the efficacy, reliability, and sensitivity of motion correction strategies for resting-state functional MRI. *Neuroimage* **171**, 415-436 (2018).

177 Muller, K. R., Mika, S., Ratsch, G., Tsuda, K. & Scholkopf, B. An introduction to kernel-based learning algorithms. *Ieee T Neural Networ* **12**, 181-201 (2001).

178 Maris, E. & Oostenveld, R. Nonparametric statistical testing of EEG- and MEG-data. *Journal of neuroscience methods* **164**, 177-190 (2007).

179 Friston, K. J., Williams, S., Howard, R., Frackowiak, R. S. & Turner, R. Movement-related effects in fMRI time-series. *Magn Reson Med* **35**, 346-355 (1996).

180 Eickhoff, S. B. *et al.* A new SPM toolbox for combining probabilistic cytoarchitectonic maps and functional imaging data. *Neuroimage* **25**, 1325-1335 (2005).

181 Krauth, A. *et al.* A mean three-dimensional atlas of the human thalamus: generation from multiple histological data. *Neuroimage* **49**, 2053-2062 (2010).

182 Hwang, K., Bertolero, M. A., Liu, W. B. & D'Esposito, M. The Human Thalamus Is an Integrative Hub for Functional Brain Networks. *The Journal of neuroscience : the official journal of the Society for Neuroscience* **37**, 5594-5607 (2017).

183 Horn, A. & Blankenburg, F. Toward a standardized structural-functional group connectome in MNI space. *Neuroimage* **124**, 310-322 (2016).

184 Loftus, G. R. & Masson, M. E. Using confidence intervals in within-subject designs. *Psychon Bull Rev* **1**, 476-490 (1994).

185 Krishnan, A., Williams, L. J., McIntosh, A. R. & Abdi, H. Partial Least Squares (PLS) methods for neuroimaging: a tutorial and review. *Neuroimage* **56**, 455-475 (2011).

186 McIntosh, A. R., Bookstein, F. L., Haxby, J. V. & Grady, C. L. Spatial pattern analysis of functional brain images using partial least squares. *Neuroimage* **3**, 143-157 (1996).

187 Efron, B. & Tibshirani, R. Bootstrap Methods for Standard Errors, Confidence Intervals, and Other Measures of Statistical Accuracy. *Statistical Science* **1**, 54-75 (1986).

Supplementary Information for

Broadscale dampening of uncertainty adjustment in the aging brain

Julian Q. Kosciessa*, Ulrich Mayr, Ulman Lindenberger, & Douglas D. Garrett*

* Email: kosciessa@mpib-berlin.mpg.de; garrett@mpib-berlin.mpg.de

This PDF file includes:

Supplementary Figures S1 to S6
Supplementary Text S1 to S6
Supplementary Table S1-5
Supplementary References

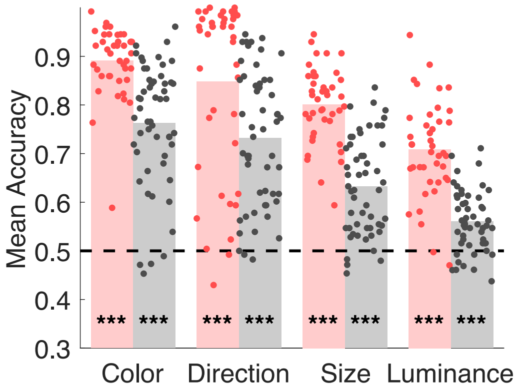

Figure S1-1. Average accuracy across target load conditions. Younger (red) and older adults (grey) performed the task above chance for all attributes that were probed. Statistics are based on one sample t-tests against chance level (.5 in this 2AFC task). *** p < .001.

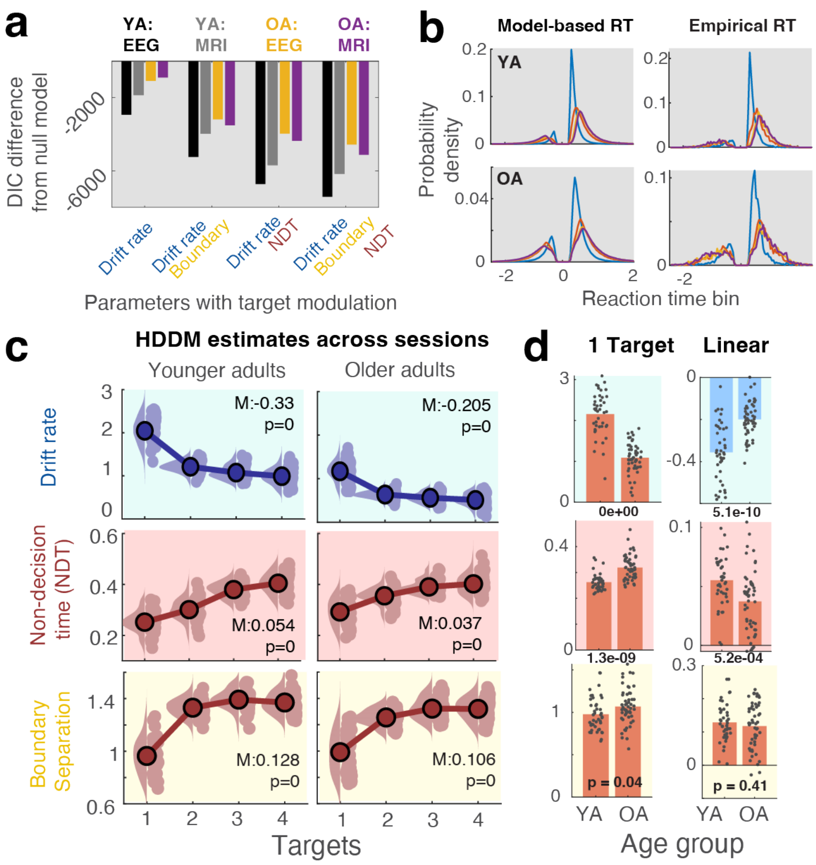

Figure S1-2. Age-related uncertainty adjustments to decision processes. (a) DIC-based model comparison indicates that a model, including uncertainty modulation of drift rates, non-decision times, and boundary separation provides the best group fit to the behavioral data. (b) Posterior predictive checks for the full model (shown for the EEG session). Negative RTs indicate incorrect responses. Model-based ("posterior predictive") values were sampled 50 times within each subject and condition (as implemented in the HDDM package), and probability density (100 RT bins) was estimated first within-subject across all samples, and then averaged across participants. In empirical data, probability densities were estimated across all participants due to the sparse within-subject RT counts. (c) Uncertainty modulation of HDD parameter estimates, averaged across sessions. Statistics refer to paired t-tests of linear slopes against zero. Data are within-subject centered. (d) Age comparison of single-target parameter estimates (left) and linear uncertainty effects (~age x target load interaction). Statistics refer to unpaired t-tests.

Text 1-2. Uncertainty and age effects on non-decision time and boundary separation. The main analyses targeted drift rate as the main parameter of interest. Given that the best-fitting model (Figure S1-2ab) included uncertainty variation also for non-decision times as well as boundary separation, we explored the potential variation of the latter two parameters with age and uncertainty (Figure S1-2c). In contrast with younger adults, older adults had significantly longer non-decision times, and larger boundary separation, suggesting that more evidence was collected prior to committing to a choice. There is some evidence from 2AFC tasks that older adults adopt decision boundaries that are wider than the boundaries of younger adults (Starns & Ratcliff, 2010, 2012) [but see (McGovern et al., 2018)], which may signify increased response caution . In both age groups, we observed uncertainty-related increases in non-decision times, albeit more constrained in older adults, as well as similar increases in boundary separation as a function of rising uncertainty (see Figure S1-2d). Notably, the uncertainty effect on boundary separation was not consistently reproduced by either the integration threshold of the domain-general CPP (Figure S1-4b), or the effector-specific contralateral beta power threshold (Figure S1-5d), highlighting uncertainty regarding the true effect on behavioral response caution, or neural proxy signatures thereof. These discrepancies deserve further attention in future work and may suggest that a model with alternative parameter constellations could provide a more coherent description. Convergence of the current model with our previous results in younger adults (Kosciessa et al., 2021) ultimately argues for robust drift rate inferences that were independent from the specific model choice.

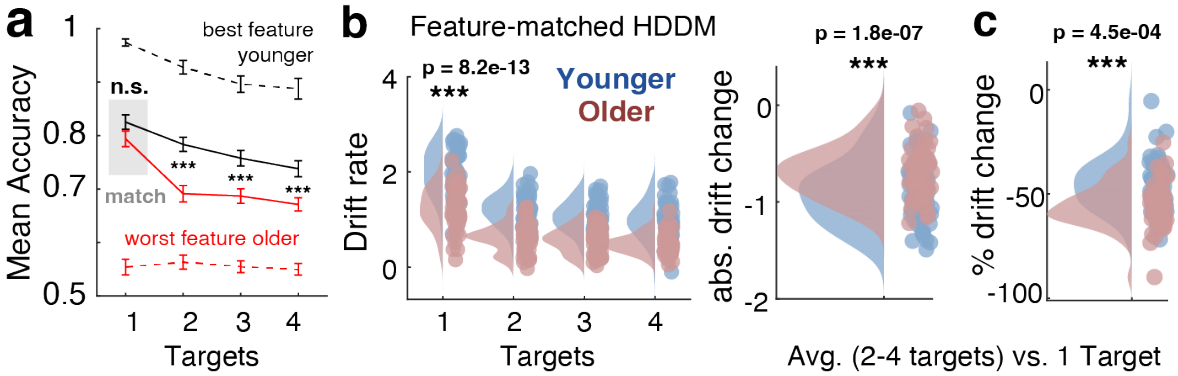

Figure S1-3. Drift rate differences do not arise from accuracy ceiling or floor effects. (**a**) Difficulty with selectively distinguishing individual features is a major component of the task, which may contribute to age differences in single-target drift rates. While on average, younger adults' single-target responses were more accurate than those of older adults, this differed between features (see Fig. S1-1). Excluding the most accurate ('best') feature for younger adults and the least accurate ('worst') feature for older adults matched groups regarding their accuracy in the single-target condition. In this scenario, older adults showed more pronounced accuracy decreases under uncertainty, relative to younger adults. Data are means +/- SEs and include data from EEG and fMRI sessions. n.s.: p = 0.13; ***1: p = 2.6e-05; ***2: p = 6.1e-04; ***3: p = 8.2e-04. (**b**) Drift rate estimates for an HDDM model that only included age-matched features ("match" in ***a***). This model indicated retained age differences in single-target drift rate and drift changes under uncertainty (right). (**c**) Older (vs. younger) adults showed stronger *relative* drift rate reductions from the single-target baseline.

Text S1-3. Drift rate effects for accuracy-matched features. Our analysis indicated that older adults on average showed reduced behavioral uncertainty costs. However, these uncertainty costs are thought to arise from attending to a varied feature set, whose discrimination also varies between age groups when only a single feature is relevant. To examine whether potential ceiling or floor effects in feature-specific accuracy (e.g., due to varying perceptual uncertainty) acts as a between-group confound, we sorted features according to their single-target accuracy in each participant, and averaged accuracy according to such " preference" within each age group. This revealed that three out of the four features elicited comparable single-target accuracy between age groups, whereas only the best feature of younger adults, and the worst feature of older adults could not be matched (Figure S1-3a). To test the robustness of unmatched drift rate estimates (Fig. 1b), we created HDDM models that excluded the most preferred feature of younger adults, and the individually least preferred feature in older adults (i.e., only including "matched" features). Results from this control analysis are shown in Figure S1-3b. We observed retained age differences in single-target drift rates, as well as uncertainty-related drift rate changes that mirrored our main results. These results indicate that baseline feature differences are likely not the principal origin of age and uncertainty drift rate differences.

Text S1-4. More pronounced relative performance decreases in older adults. Compared with younger adults, older adults' drift rates were lower across levels of target load (Fig. 1b). To probe whether drift rates across all set sizes show similar proportional age changes, we calculated relative drift rate changes. Arguing against uncertainty-independent age differences in drift rate, we observed larger *relative* drift rate decreases under uncertainty in older as compared with younger adults (see Fig. S1-3b right for feature-matched HDDM; similar results were obtained in the main model). This indicates that despite being smaller in absolute terms, older as compared to younger adults suffered stronger *relative* drift rate losses once uncertainty was introduced. This mirrored larger accuracy decreases in matched features once uncertainty was introduced (Fig. S1-3a). Taken together, this indicates that uncertain contexts present an outsized challenge to older adults' performance, over and above challenges in single-target specificity. For our main analyses that target inter-individual relations, we focus on absolute uncertainty-related drift rate changes due to their relation to neural uncertainty adjustment in prior work (Kosciessa et al., 2021), and the computational interpretability of absolute drift rates at each target load.

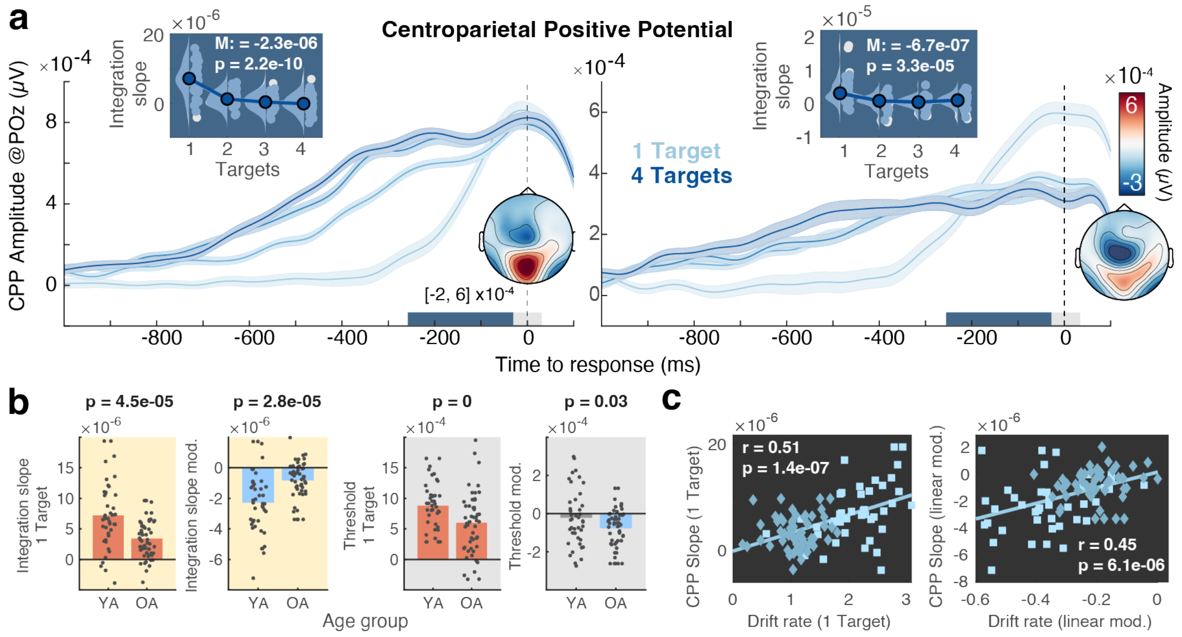

Figure S1-4. Centroparietal Positive Potential (CPP) as a signature of domain-general evidence integration. (a) Modulation of CPP as a neural signature of evidence accumulation (mean ± within-subject SEM). The integration slope of the response-locked CPP decreases with increasing probe uncertainty. Traces are mean ± within-subject SEM. Insets show CPP slope estimates from −250 to −50 ms relative to response execution. (b) Age comparison of CPP integration slopes (yellow background) and CPP integration thresholds (grey backgrounds). (c) CPP estimates of evidence integration converge with behavioral drift rate estimates at the interindividual level, both w.r.t the single-target condition (r(93) = 0.45, 95%CI = [0.27,0.59], p = 6.1e-06; *age-partialed*: r(92) = 0.27, 95%CI = [0.08,0.45] p = 0.01) and linear effects of target number (r(93) = 0.51, 95%CI = [0.34,0.64], p = 1.4e-07; *age-partialed*: r(92) = 0.34, 95%CI = [0.14,0.5] p = 9.3e-04).

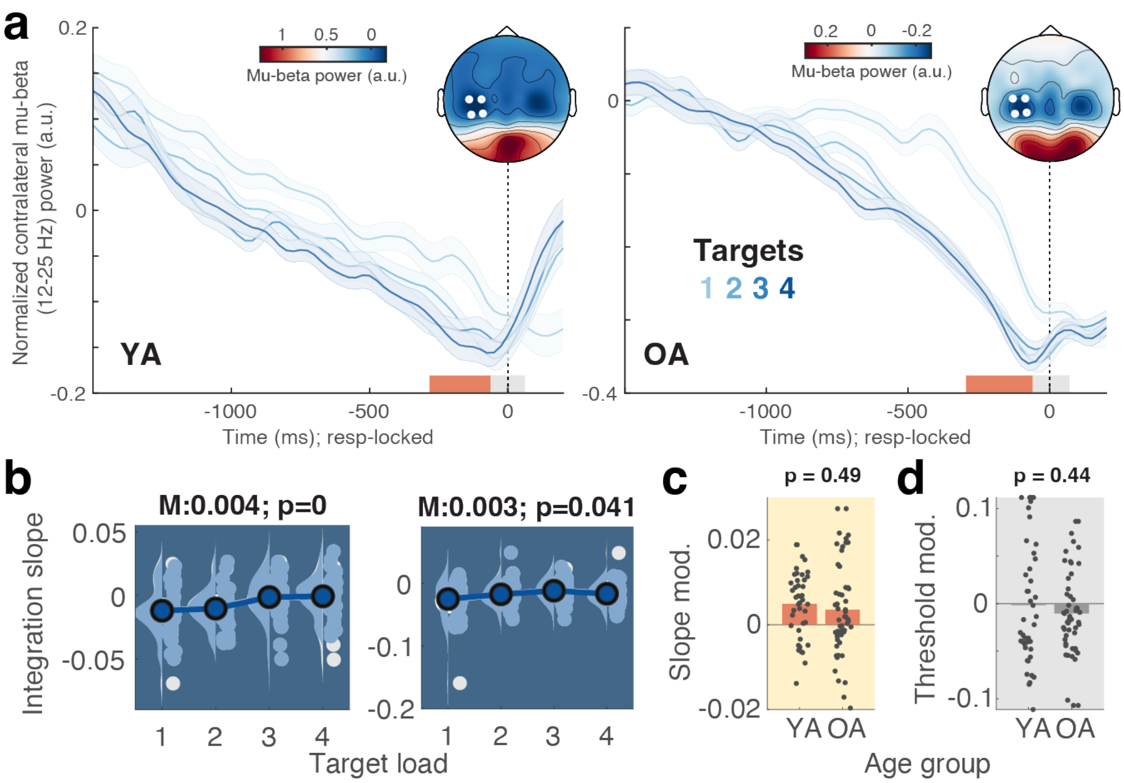

Figure S1-5. Contralateral beta power as a signature of motor-specific response preparation. (a) Pre-response desynchronization of contralateral mu-beta power shallow with increasing number of targets. Traces show means +/- within-subject SEM. (b) Linear slope estimates, estimated via linear regression from -250 ms to -50 ms, relative to response. Data are within-subject centered for visualization. Statistics refer to paired t-tests of linear slopes against zero. (c, d) Age comparison of linear modulation of beta slopes (c) and integration thresholds (d) by target load. Statistics refer to unpaired t-tests.

Text 1-5. Motor-specific response preparation. In addition to the domain-general CPP, we also investigated motor-specific contralateral beta power (Figure S1-5a). Extending results from behavioral modeling, and CPP integration slopes, we observed a shallowing of pre-response beta power build-up, suggesting decreases in response preparation (Figure S1-5b). However, such shallowing was not statistically different between age groups (Figure S1-5b), thus deviating from the age x load interaction that we observed for the remaining integration signatures. Furthermore, linear changes in beta slope as a function of target load were neither associated with linear drift changes ($r(93) = -0.03$, 95%CI = [-0.23,0.17], $p = 0.77$) nor CPP slopes ($r(93) = -0.11$, 95%CI = [-0.3,0.09], $p = 0.29$) across age groups. The parameters were also not directly related in the single-target condition (*drift rates*: $r(93) = 0.18$, 95%CI = [-0.02,0.37], $p = 0.07$; *CPP slopes*: $r(93) = -0.06$, 95%CI = [-0.26,0.14], $p = 0.55$). Motor-specific response preparation thus appears to partially dissociate from effector-unspecific evidence integration at the individual level.

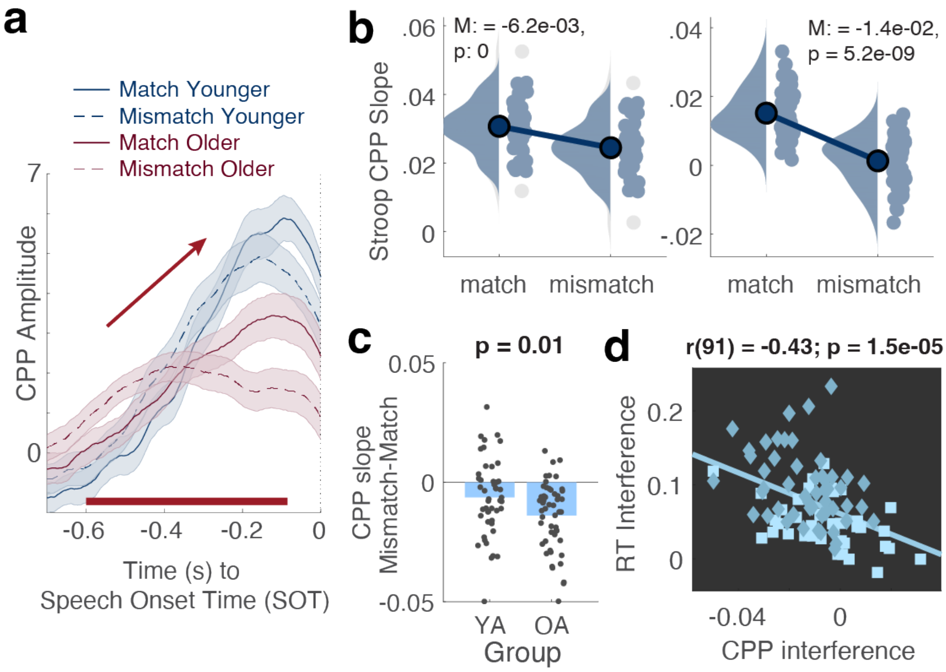

Figure S3-1. CPP slope during the Stroop task. (a) Response-aligned CPP traces split by condition and age group. Time series were smoothed with 60 ms windows for visualization, but not for slope fitting. Linear slopes were estimated during the interval of -600 to -100 ms prior to indicated SOTs, marked by the red line. (a) CPP integration slopes were reduced in magnitude in the mismatch condition in both age groups. (b) Interference effects on CPP slopes were more pronounced in younger ad compared with older adults. The magnitude of individual interference effects was similarly reflected in RTs and CPP slopes with longer RTs being coupled to stronger CPP slope reductions [r(91) = -0.43, 95%CI = [-0.58,-0.25], p = 1.5e-05; partial-correlation accounting for age: r(89) = -0.32, 95%CI = [-0.49,-0.12] p = 3.3e-04].

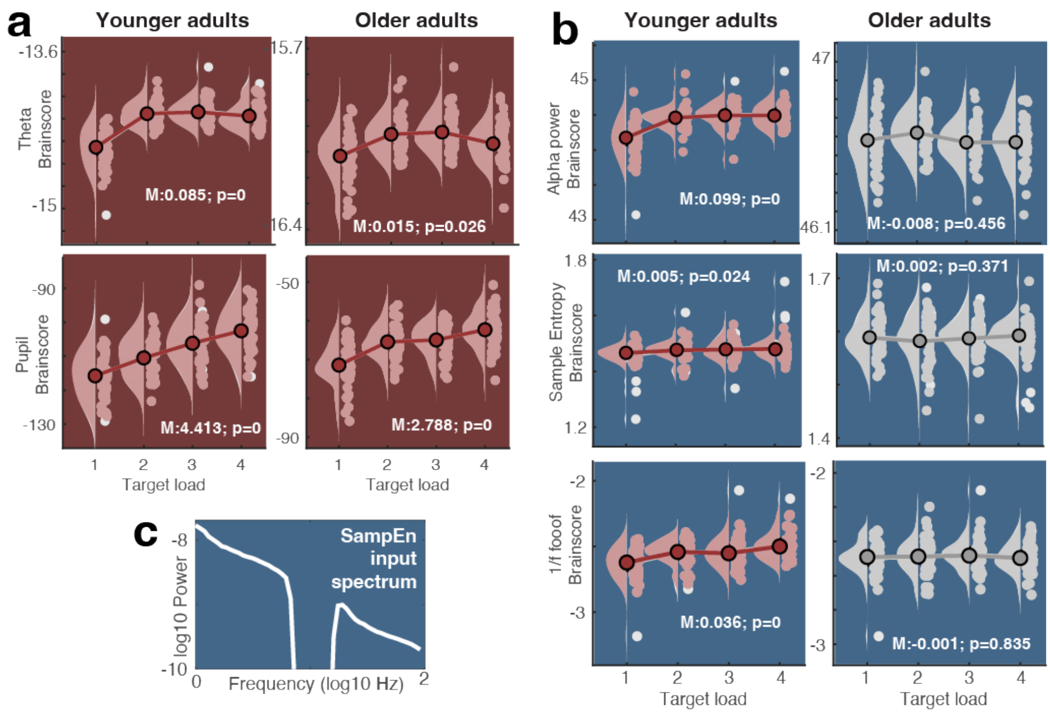

Figure S4-1. Load modulation for cognitive control (a) and excitability signatures (b). Statistics refer to paired t-tests of linear slopes against zero. In line with the different excitability indices capturing a shared latent characteristic, the magnitude of uncertainty modulation was inter-individually related among the three parameters (alpha-1/f: $r = 0.44$, $p = 9.8e\text{-}06$; 1/f-SampEn: $r = 0.6$, $p = 1.1e\text{-}10$; SampEn-alpha: $r = 0.24$, $p = .02$). (c) Sample entropy input spectrum highlighting the exclusion of alpha-range signal content.

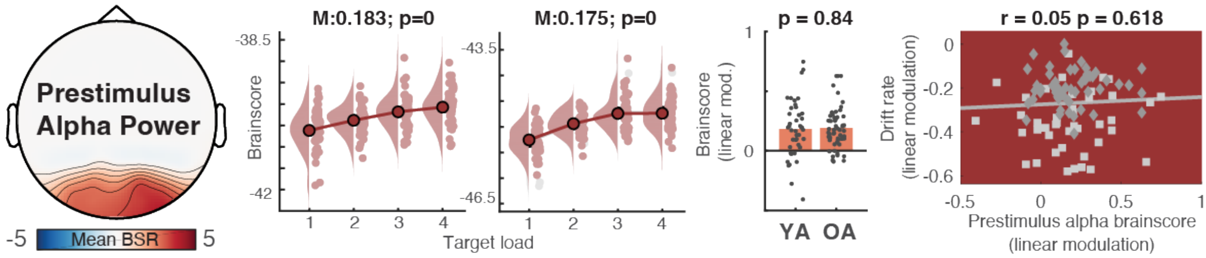

Figure S5-1. Pre-stimulus alpha power. Uncertainty similarly increases pre-stimulus alpha power in younger and older adults but does not relate to individual drift rate adjustments. Light grey squares indicate younger adults, dark grey diamonds correspond to older adults.

Text S5-1 Pre-stimulus alpha power. Evidence on age-related changes in pre-stimulus alpha power are mixed. Early studies suggest that pre-stimulus alpha synchronization (or lateralization) in the context of attentional cueing is observed exclusively for younger, but not older adults (Hong et al., 2015; Vaden et al., 2012). In contrast, (Leenders et al., 2018) indicated similar pre-stimulus lateralization between age groups, whereas they noted age differences in alpha modulation during working memory retention. While our task design does not allow us to assess the lateralization of alpha power, our results indicate that pre-stimulus alpha power increases similarly alongside uncertainty in both age groups, but with no apparent relation to subsequent (delayed) task performance (Figure S3-1).

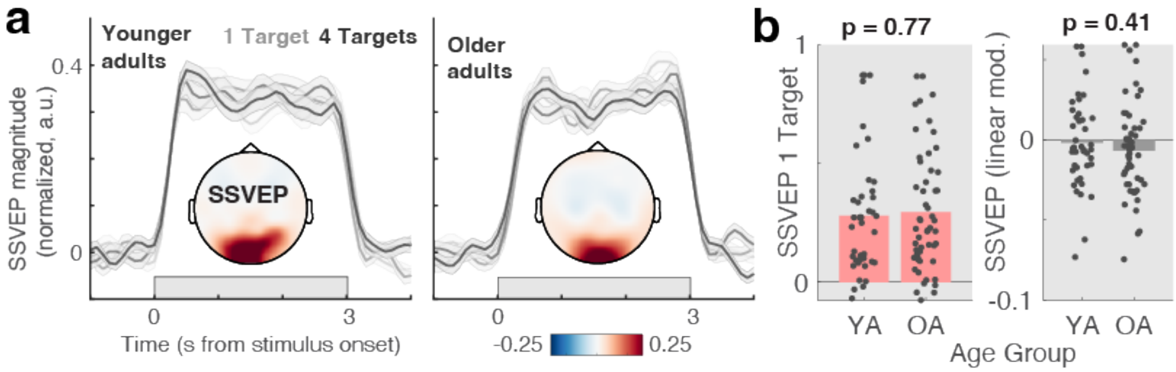

Figure S5-2. Steady-state visual evoked potential (SSVEP). (a) Both age groups exhibited a robust SSVEPs. Time-resolved, spectrally normalized, SSVEP power, averaged across occipital channels (O1, Oz, O2), indicates clear SSVEP increases specifically during stimulus presentation. Data are presented as mean values +/- within-subject SEM. Topography insets show stimulus-evoked SSVEP contrast minus baseline. (b) However, estimates from occipital EEG channels (O1, Oz, O2) did not indicate age differences in single-target SSVEP magnitude, a main effect of load in either group, or differences in the strength of linear modulation (~ age*load interaction).

Text S5-2. SSVEP magnitude. SSVEP magnitude has been suggested as a signature of encoded sensory information that is enhanced by attention (Morgan et al., 1996; Muller et al., 2006; Quigley et al., 2010; Quigley & Muller, 2014) and indicates fluctuations in early visual cortex excitability (Zhigalov et al., 2019). However, despite a clear SSVEP signature of comparable magnitude in both younger and older adults (Fig. S5-2 a, b), we did not observe significant effects of target uncertainty on SSVEP magnitude in either age group (Fig. S5-2). Given that the SSVEP frequency was shared across different features, we could not investigate feature selection via SSVEPs as is commonly the case in attention studies. Studies with feature-specific SSVEPs, suggest that younger adults' SSVEP magnitude differentiates between attended and unattended features, whereas no robust differentiation is observed in older adults, pointing to deficits in attentional filtering (Quigley et al., 2010; Quigley & Muller, 2014).

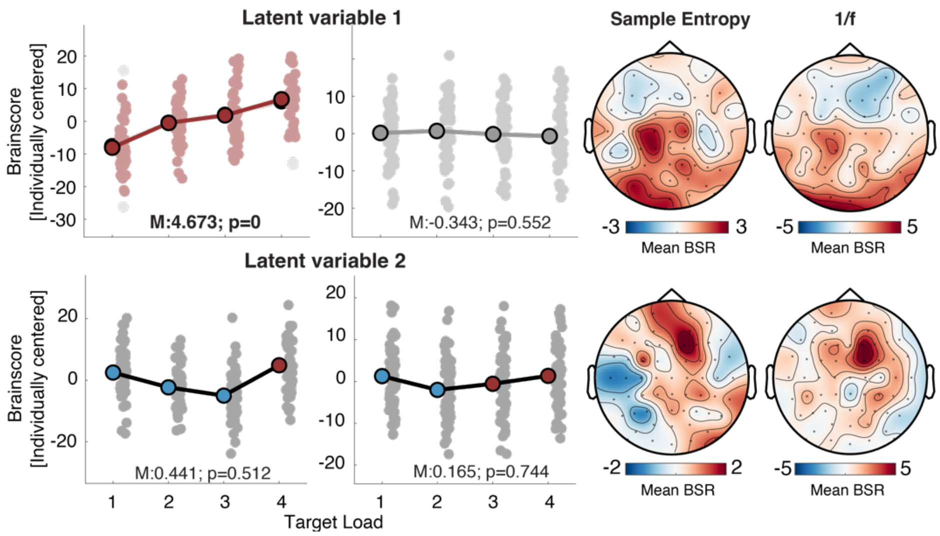

Figure S5-3. Task PLS of sample entropy and aperiodic slopes across all channels. Brainscores for younger adults are shown on the left side, with data for older adults shown to the right. Inset estimates refer to fixed linear effects models. Topographies of bootstrap ratios are unthresholded.

Text S5-3. Exploratory whole-brain task PLS of aperiodic dynamics. In the main analysis, we restricted the PLS to posterior channels with the aim to predominantly characterize signals stemming from parietal and visual cortex. To explore whether this analysis missed uncertainty-related changes in aperiodic dynamics in other regions, we performed an additional task PLS analysis that included all channels. This task PLS averaged sample entropy across the final 2.5s of stimulus presentation. To normalize relative contributions of the two signatures to the PLS, we z-transformed values of each signature across target load levels prior to including them in the model. This joint PLS resulted in two significant latent variables (Figure S5-3). The first latent variable (*permuted* $p = 0.001$) indicated uncertainty-related increases in sample entropy and shallowing of aperiodic slopes in younger, but not older adults. Regional contributions were predominantly observed in posterior sensors. This latent variable thus captures the observations in the main analysis. The second latent variable (*permuted* $p = 0.021$) was instead marked by quadratic changes (younger adults: $p = 1.5e\text{-}08$; older adults: $p = 0.03$; linear mixed effects model with fixed and random quadratic effects) as a function of target load. Estimates initially decreased, followed by an increase with load towards higher target load, predominantly at mediofrontal channels.

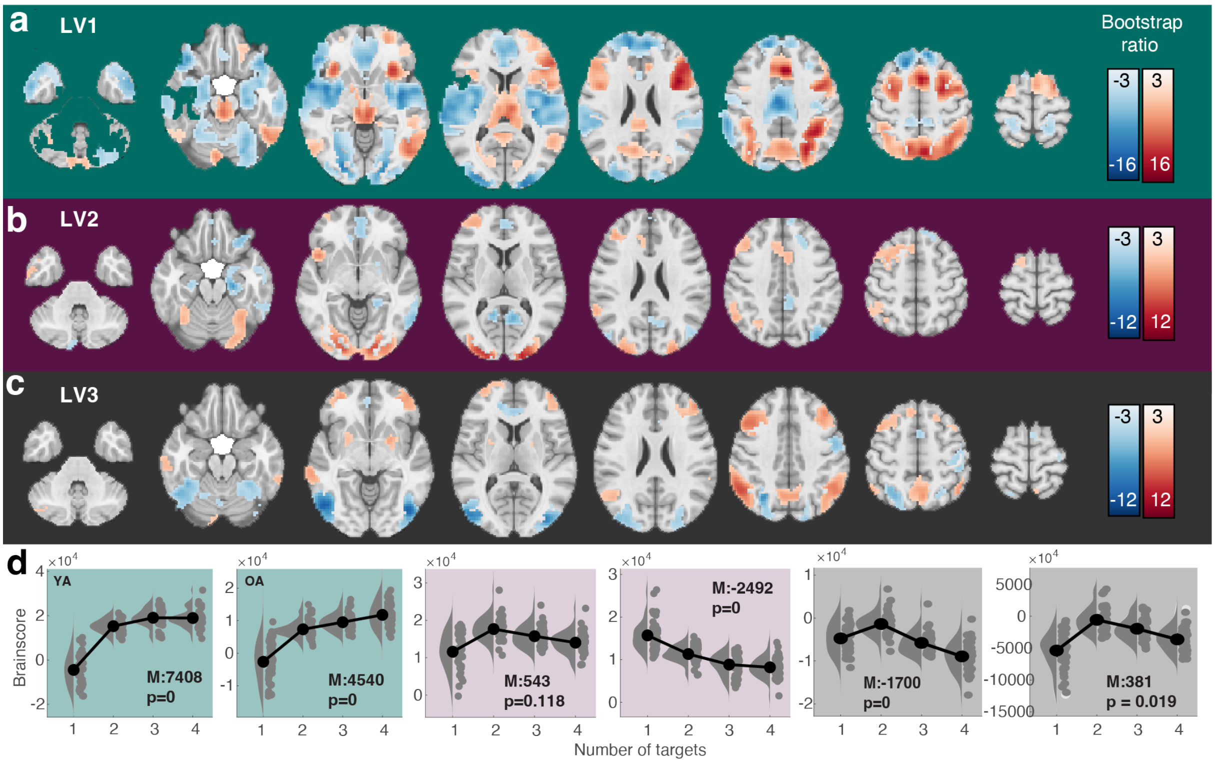

Figure S6-1. Main effects of target load on BOLD magnitude. A task partial least squares (PLS) analysis indicated three significant latent variables (loadings shown in panels a-c) that were sensitive to changes in target number. (d) Statistics refer to paired t-tests of linear slopes against zero.

Text S6-1. Main effects of uncertainty on BOLD magnitude across the adult lifespan. We performed a whole-brain task PLS to assess potential main effects of uncertainty on BOLD magnitude. In brief, we observed a similar first latent variable (*permuted* $p < 0.001$) to that reported in younger adults (Kosciessa et al., 2021), highlighting uncertainty-related increases dominantly in cortical areas encompassing the frontoparietal and the midcingulo-insular network, as well as in the thalamus (see detailed results of this analysis in Figure S6-1 and Table S2-4.The task PLS indicated two further robust LVs. LV2 (*permuted* $p < 0.001$) captured a non-linear pattern in younger adults and linear changes under uncertainty in older adults. Regional contributors partly overlapped with the initial LV (Table S3). Finally, LV3 (*permuted* $p < 0.001$) captured nonlinear changes (initial increases in engagement followed by disengagement) in both age groups in a set of regions encompassing positive loadings in frontoparietal components of the executive control network, and negative loadings in temporal-occipital cortex (Table S4).

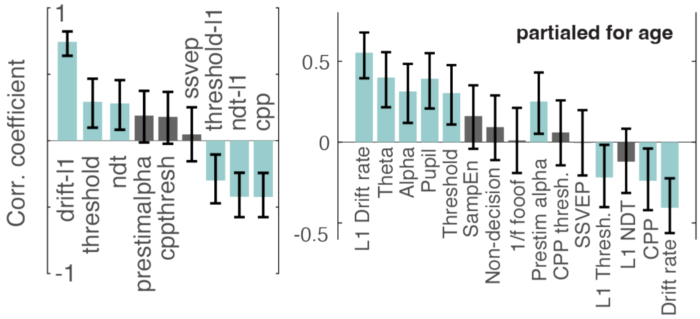

Figure S6-2. Additional brainscore relations before (left) and after controlling for categorical age (right). Beyond the *a priori* signatures included in the behavioral PLS model, post-hoc exploration indicated that individuals with more pronounced BOLD uncertainty modulation also had larger single-target drift rates, and lower single-target boundary separation ("boundary thresholds"), as well as larger increases in the latter as a function of uncertainty, also after controlling for categorical age (see right). In addition to the magnitude of uncertainty-related drift rate modulation, CPP slope modulation was similarly related to Brainscores. Plots indicate Pearson correlation coefficients +- 95%CI after accounting for age covariation.

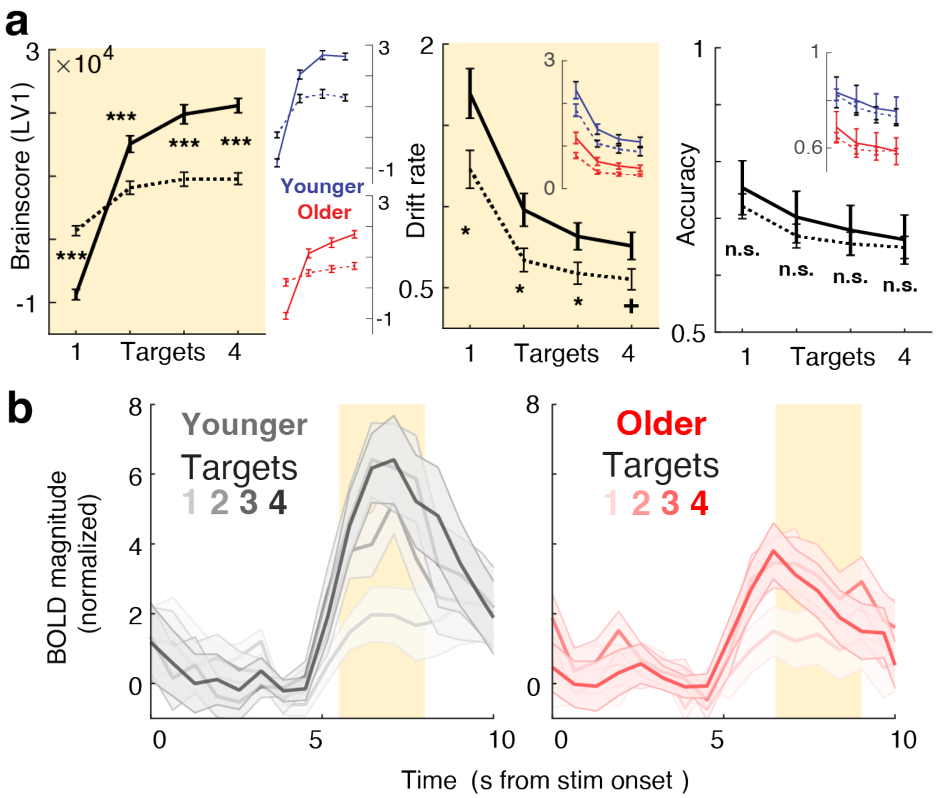

Figure S6-3. BOLD modulation effects are robust to accuracy differences within (a) and between age groups (b). (a) Younger and older individuals with larger BOLD uncertainty modulation (LV1, see Fig S6-1) achieve higher drift rates across uncertainty levels at comparable accuracy levels. Data show upper (full lines) and lower (broken lines) groups of a trichotomized split of accuracy and drift rate data based on the magnitude of uncertainty change (234 vs. 1) in the 1st LV of the task PLS (closely mirroring the change LV1 of the behavioral PLS). Insets illustrate comparable within-group splits (split performed within-group). Data are means +- SEs. (b) Age x uncertainty interaction in mediodorsal thalamus for accuracy-matched features. For this analysis, trials with probes of the best (YA) or worst (OA) features were excluded to achieve group-matched single-target accuracy (see Text S1-3). A linear mixed effects model indicated a retained group x target load interaction for data averaged in the time window of interest (yellow shading; beta=-0.757, SE=0.369, t = -2.0507, dof = 364, p = 0.041, 95%CI = [-1.48, -0.03]). Data are means +- SEs.

Table S1: Statistics for within age-group effects. Effects were assessed via paired t-tests against zero. YA: Younger adults. OA: Older adults.

Dependent variable	Figure	df	t-value	p-value	Cohen's d
Drift rate (single-target) – YA	1b	41	26.41	2.3e-27	4.07
Drift rate (single-target) – OA	1b	52	22.06	4.6e-28	3.03
CPP (single-target) – YA	1b	41	8.62	9.5e-11	1.33
CPP (single-target) – OA	1b	52	7.92	1.7e-10	1.09
Drift rate (linear mod.) – YA	1b	41	-17.07	3.1e-20	-2.63
Drift rate (linear mod.)) – OA	1b	52	-17.45	2.2e-23	-2.4
CPP (linear mod.)) – YA	1b	41	-7.37	4.9e-09	-1.14
CPP (linear mod.)) – OA	1b	52	-5.04	5.9e-06	-0.69
Stroop interference – YA	3b	47	10.01	3.1e-13	1.44
Stroop interference – OA	3b	52	16.02	9.3e-22	2.2
Theta power (linear mod.) – YA	4a	41	6.85	2.6e-08	1.06
Theta power (linear mod.) – OA	4a	52	2.3	2.6e-02	0.32
Pupil diameter (linear mod.) – YA	4b	41	7.34	5.6e-09	1.13
Pupil diameter (linear mod.) – OA	4b	52	7.25	1.9e-09	1
Alpha power (linear mod.) – YA	5a	41	6.05	3.7e-07	0.93
Alpha power (linear mod.) – OA	5a	52	-0.75	0.46	-0.1
Sample Entropy (linear mod.) – YA	5b	41	2.21	0.033	0.34
Sample Entropy (linear mod.) – OA	5b	52	0.23	0.82	0.03
1/f slope (linear mod.) – YA	5c	41	4.67	3.3e-05	0.72
1/f slope (linear mod.) – OA	5c	52	0.14	0.89	0.02
fMRI Brainscore – YA	6b	41	11.49	2.1e-14	1.77
fMRI Brainscore – OA	6b	52	7.47	8.8e-10	1.03

Table S2: PLS model peak activations, bootstrap ratios, and cluster sizes for task PLS LV1.

		MNI Coordinates				
Region	Hem	X	Y	Z	BSR	#Voxels
IFG (p. Opercularis)	L	-45	9	27	15.11	3164
Inferior Parietal Lobule	L	-42	-48	45	14.3	3451
Insula Lobe	R	30	21	-3	11.4	170
Inferior Temporal Gyrus	L	-54	-66	-12	11.34	880
Thalamus	L	-6	-30	-3	10.76	1064
Superior Frontal Gyrus	R	27	-3	54	10.21	903
Cerebelum (Crus 1)	R	6	-81	-24	8.5	276
Cerebelum (VI)	R	30	-66	-30	7.83	129
Inferior Temporal Gyrus	R	54	-63	-12	6.19	297
Area Fo3	L	-27	39	-21	4.68	45
Calcarine Gyrus	L	-15	-78	6	4.28	29
Middle Frontal Gyrus	R	27	51	3	4.25	31
Superior Medial Gyrus	R	12	48	33	-12.32	2317
Area hOc3d [V3d]	L	-24	-99	12	-11.64	6542
MCC	R	3	-15	36	-11.23	889
Area lg1	R	30	-21	3	-11.14	4238
Postcentral Gyrus	R	21	-36	63	-5.86	121
Postcentral Gyrus	L	-39	-21	36	-5.8	43
Middle Frontal Gyrus	L	-33	24	39	-5.32	32
Angular Gyrus	L	-48	-63	27	-4.81	59
Middle Frontal Gyrus	R	45	15	48	-3.95	55

Table S3: PLS model peak activations, bootstrap ratios, and cluster sizes for task PLS LV2.

		MNI Coordinates				
Region	Hem	X	Y	Z	BSR	#Voxels
Area hOc3d [V3d]	L	-24	-99	12	9.16	1974
Insula Lobe	R	42	15	-3	6.66	136
Middle Orbital Gyrus	R	30	54	-15	5.31	143
Superior Frontal Gyrus	R	21	12	60	5.01	911
Middle Frontal Gyrus	R	33	48	12	4.91	119
Angular Gyrus	R	57	-51	27	4.76	280
Inferior Temporal Gyrus	R	51	-3	-39	4.47	50
Inferior Temporal Gyrus	R	63	-27	-30	4.4	28
Superior Occipital Gyrus	R	21	-63	42	4.05	69
Rolandic Operculum	L	-57	6	3	3.79	27
Hippocampus	L	-27	-21	-18	-7.36	316
Calcarine Gyrus	L	-12	-60	12	-6.5	244
Rectal Gyrus	L	-9	27	-15	-6.24	440
Middle Temporal Gyrus	L	-66	-57	-9	-6.12	256
Middle Occipital Gyrus	L	-42	-81	39	-6.08	190
IFG (p. Orbitalis)	L	-36	33	-18	-5.97	94
Precuneus	R	9	-54	9	-5.67	131
ParaHippocampal Gyrus	R	21	-21	-18	-4.83	39
IFG (p. Orbitalis)	R	24	27	-15	-4.67	28
Middle Temporal Gyrus	R	54	-6	-15	-4.56	51
MCC	L	-12	-42	36	-4.44	76
Middle Occipital Gyrus	R	45	-78	27	-4.34	34
Middle Frontal Gyrus	L	-27	30	42	-4.27	153
Cerebelum (Crus 2)	R	3	-87	-33	-4.14	28
Middle Temporal Gyrus	L	-51	-3	-24	-3.94	53
Superior Frontal Gyrus	L	-24	60	3	-3.78	27

Table S4: PLS model peak activations, bootstrap ratios, and cluster sizes for task PLS LV3.

		MNI Coordinates				
Region	Hem	X	Y	Z	BSR	#Voxels
Angular Gyrus	R	51	-57	36	8.05	604
Middle Frontal Gyrus	R	36	21	36	6.87	660
Inferior Parietal Lobule	L	-54	-51	42	6.27	469
Precuneus	L	-9	-66	45	6.13	474
Middle Frontal Gyrus	L	-39	24	33	6.05	726
Middle Frontal Gyrus	R	27	57	0	5.97	287
Middle Temporal Gyrus	R	60	-33	-12	5.46	184
Cerebelum (Crus 1)	R	9	-81	-27	5.29	62
Putamen	L	-27	6	-6	4.82	74
Putamen	R	24	0	6	4.38	67
Inferior Temporal Gyrus	L	-66	-42	-21	4.16	49
Cerebelum (Crus 2)	L	-15	-87	-30	3.96	32
Cerebelum (Crus 2)	R	33	-72	-45	3.8	53
Inferior Temporal Gyrus	R	48	-69	-9	-10.33	1706
Inferior Occipital Gyrus	L	-45	-75	-6	-9.9	1022
Postcentral Gyrus	L	-57	-6	39	-5.18	232
Postcentral Gyrus	L	-51	-33	57	-4.5	43
ACC	R	12	42	9	-4.41	191
Superior Parietal Lobule	L	-24	-63	48	-4.4	36
Posterior-Medial Frontal	L	-6	3	57	-4.4	65

Table S5: PLS model peak activations, bootstrap ratios, and cluster sizes for behavioral PLS LV1.

		MNI Coordinates				
Region	Hem	X	Y	Z	BSR	#Voxels
Thalamus	L	-6	-15	12	8.57	573
Posterior-Medial Frontal	L	3	12	45	8.13	555
Precentral Gyrus	L	-42	0	30	7.51	931
Superior Frontal Gyrus	R	27	-3	54	6.91	222
Inferior Occipital Gyrus	L	-42	-72	-6	6.13	208
Middle Temporal Gyrus	L	-51	-51	21	6.03	90
Putamen	R	30	18	0	5.75	94
Middle Frontal Gyrus	R	36	24	21	5.74	220
Middle Temporal Gyrus	L	-57	-33	-6	5.26	35
Inferior Parietal Lobule	R	30	-54	48	5.14	323
Inferior Parietal Lobule	L	-36	-57	45	4.75	315
Area hOc1 [V1]	R	9	-99	6	4.7	82
Inferior Temporal Gyrus	R	45	-63	-12	4.51	27
Hippocampus	L	-27	-18	-21	-8.92	873
MCC	L	-12	-36	48	-6.05	359
Putamen	R	30	-3	9	-5.79	879
Superior Frontal Gyrus	R	18	54	30	-5.73	443
Middle Frontal Gyrus	L	-21	30	54	-5.45	67
Superior Medial Gyrus	R	12	42	48	-5.28	138
IFG (p. Orbitalis)	R	36	30	-21	-5.2	55
ParaHippocampal Gyrus	R	21	-18	-18	-5.13	49
Middle Temporal Gyrus	L	-51	3	-33	-4.28	29
Inferior Frontal Gyrus	L	-33	36	-21	-4.17	26
Rectal Gyrus	L	-9	24	-12	-4.15	73
Inferior Temporal Gyrus	L	-57	-24	-27	-4.03	32

Supplementary References

Hong, X. F., Sun, J. F., Bengson, J. J., Mangun, G. R., & Tong, S. B. (2015). Normal aging selectively diminishes alpha lateralization in visual spatial attention. *NeuroImage*, *106*, 353-363. https://doi.org/10.1016/j.neuroimage.2014.11.019

Kosciessa, J. Q., Lindenberger, U., & Garrett, D. D. (2021). Thalamocortical excitability modulation guides human perception under uncertainty. *Nature Communications*, *12*(1), 2430. https://doi.org/10.1038/s41467-021-22511-7

Leenders, M. P., Lozano-Soldevilla, D., Roberts, M. J., Jensen, O., & De Weerd, P. (2018). Diminished Alpha Lateralization During Working Memory but Not During Attentional Cueing in Older Adults. *Cereb Cortex*, *28*(1), 21-32. https://doi.org/10.1093/cercor/bhw345

McGovern, D. P., Hayes, A., Kelly, S. P., & O'Connell, R. G. (2018). Reconciling age-related changes in behavioural and neural indices of human perceptual decision-making. *Nat Hum Behav*, *2*(12), 955-966. https://doi.org/10.1038/s41562-018-0465-6

Morgan, S. T., Hansen, J. C., & Hillyard, S. A. (1996). Selective attention to stimulus location modulates the steady-state visual evoked potential. *Proc Natl Acad Sci U S A*, *93*(10), 4770-4774. https://doi.org/10.1073/pnas.93.10.4770

Muller, M. M., Andersen, S., Trujillo, N. J., Valdes-Sosa, P., Malinowski, P., & Hillyard, S. A. (2006). Feature-selective attention enhances color signals in early visual areas of the human brain. *Proc Natl Acad Sci U S A*, *103*(38), 14250-14254. https://doi.org/10.1073/pnas.0606668103

Quigley, C., Andersen, S. K., Schulze, L., Grunwald, M., & Muller, M. M. (2010). Feature-selective attention: evidence for a decline in old age. *Neurosci Lett*, *474*(1), 5-8. https://doi.org/10.1016/j.neulet.2010.02.053

Quigley, C., & Muller, M. M. (2014). Feature-selective attention in healthy old age: a selective decline in selective attention? *J Neurosci*, *34*(7), 2471-2476. https://doi.org/10.1523/JNEUROSCI.2718-13.2014

Starns, J. J., & Ratcliff, R. (2010). The effects of aging on the speed-accuracy compromise: Boundary optimality in the diffusion model. *Psychol Aging*, *25*(2), 377-390. https://doi.org/10.1037/a0018022

Starns, J. J., & Ratcliff, R. (2012). Age-related differences in diffusion model boundary optimality with both trial-limited and time-limited tasks. *Psychon Bull Rev*, *19*(1), 139-145. https://doi.org/10.3758/s13423-011-0189-3

Vaden, R. J., Hutcheson, N. L., McCollum, L. A., Kentros, J., & Visscher, K. M. (2012). Older adults, unlike younger adults, do not modulate alpha power to suppress irrelevant information. *NeuroImage*, *63*(3), 1127-1133. https://doi.org/10.1016/j.neuroimage.2012.07.050

Zhigalov, A., Herring, J. D., Herpers, J., Bergmann, T. O., & Jensen, O. (2019). Probing cortical excitability using rapid frequency tagging. *NeuroImage*, *195*, 59-66. https://doi.org/10.1016/j.neuroimage.2019.03.056